UNIVERSIDAD DE CONCEPCIÓN
FACULTAD DE CIENCIAS FÍSICAS Y MATEMÁTICAS

Dense gas kinematics in the massive G351.77 protocluster ALMA-IMF Large Program observations of N_2H^+

Cinemática del gas denso en el protocúmulo masivo G351.77
Observaciones del ALMA-IMF Large Program de N_2H^+

By: Nicolás Antonio Sandoval Garrido

Thesis presented to the Facultad de Ciencias Físicas y Matemáticas de la Universidad de Concepción to grant grade of Master in astronomy.

Marzo 2024
Concepción, Chile

Profesor Guia: Amelia Marie Stutz

A Fundación 42

AGRADECIMIENTOS

Resumen

El ALMA-IMF Large Program observó 15 protocúmulos masivos en la Bandas 3 y 6, capturando multiples lineas y emisiones de continuo. Aquí estudiamos el protocumulo filamentoso masivo G351.77, ubicado a una distancia de 2 kpc. Trazamos la emisión del gas denso y la cinemática a través de la línea N_2H^+ (1-0) de 3 mm. Para recuperar la emisión, combinamos y reducimos los arreglos de 12m y 7m para luego fusionarlos con los datos de Total Power, obteniendo una imagen que captura la emisión de N_2H^+ sobre el protocúmulo a una resolución de $\sim$ 4 kUA. Modelamos el perfil de línea hiperfina de N_2H^+ con PySpecKit con dos componentes de velocidad, obteniendo el excitation temperature (T_{ex}), optical depth (τ), centroid velocity (v), y line width ($\sigma(V)$) para cada componente. En combinación con el optical depth y un mapa de columna de densidad de H_2 derivado de los datos de 1.3 mm, medimos la abundancia relativa de N_2H^+ $\sim$ $(1.66 \pm 0.46) \times 10^{-10}$. Estimamos una masa total de H_2 $\sim$ 1660 $\pm$ 458 $M_\odot$ derivado de la emisión de N_2H^+ en el protocúmulo. Examinando los diagramas de posición-velocidad a pequeñas escalas, observamos claras señales de inflow asociados a los cores de la banda de 1.3 mm. En algunos casos, señales similares fueron observadas sin cores detectados, sugiriendo la existencia de cores por debajo del límite de detección de la banda de 1.3 mm. La señal más prominente, con forma de "V" (V-shape), tiene un promedio de mass inflow rate $\sim 4.08 \times 10^{-4}$ $M_\odot$/yr y un promedio en timescale $\sim$ 20.92 kyr. Nuestro analisís revela que multiples componentes de velocidad impregnan el protocúmulo, lo que indica una compleja cinemática en el gas denso. El diagrama de posición-velocidad a grandes escalas muestra que el filamento que hospeda al protocúmulo es separado en 2 estructuras de velocidad, las cuales parecen estar rotando entre si, mientras fluyen hacia regiones más densas de N_2H^+. Además, sus timescales de acumulación de masa alcanzan $\sim$ 20 kyr.

Keywords – Protocluster - Milky Way - Kinematics - Star formation

Abstract

The ALMA-IMF Large Program observed 15 massive protoclusters in Band 3 and 6, capturing multiple lines and continuum emission. Here we study the massive filamentary protocluster G351.77, located at a distance of 2 kpc. We trace the dense gas emission and kinematics via the N_2H^+ (1-0) 3 mm line. To recover the emission, we combine and reduce the 12m-array and 7m-array to then be feathered with Total Power data, obtaining an image that captures the N_2H^+ emission over the protocluster at $\sim$ 4 kAU resolution. We model the N_2H^+ hyperfine line profile with PySpecKit with two velocity components, obtaining the excitation temperature (T_{ex}), optical depth (τ), centroid velocity (v), and line width ($\sigma(V)$) for each component. In combination with the optical depth and an H_2 column density map derived from the 1.3 mm data, we measure the N_2H^+ relative abundance $\sim$ (1.66 $\pm$ 0.46) $\times$ 10^{-10}. We estimate a total H_2 mass $\sim$ 1660 $\pm$ 458 $M_\odot$ derived from the N_2H^+ emission in the protocluster. By examining the position-velocity diagrams at small scales, we observe clear inflow signatures associated with 1.3 mm band cores. In some cases, similar signatures were observed without detected cores, suggesting the existence of cores below the 1.3 mm band detection limit. The most prominent signature, shaped like a "V" (V-shape), has an average of mass inflow rate $\sim$ 4.08 $\times$ 10^{-4} $M_\odot$/yr and an average timescale $\sim$ 20.92 kyr. Our analysis reveals that multiple velocity components pervade the protocluster, indicating kinematic complexity in the dense gas. The large-scale position-velocity diagram shows that the filament hosting the protocluster is separated into 2 velocity structures, which appear to be rotating around each other, while they inflow towards denser N_2H^+ regions. Additionally, their mass buildup timescales that reach $\sim$ 20 kyr.

Keywords – Protocluster - Milky Way - Kinematics - Star formation

Contents

List of Tables

List of Figures

Chapter 1

Introduction

The ALMA-IMF Large Program[1] observed 15 massive (2.5 - 33 $\times$ 10^3 $M_\odot$) and nearby (2 - 5.5 kpc) protoclusters in the Milky Way down to $\sim$ 2 kAU resolution, with the main goal of understanding the origin of stellar masses. The ALMA-IMF Large Program utilized the 12m-array, 7m-array and Total Power (TP) antennas of the Atacama Large Millimeter/submillimeter Array (ALMA), employing the 1.3 mm and 3 mm bands. This provides observations of continuum images and spectral lines (Motte et al., 2022; Ginsburg et al., 2022a). The 15 protoclusters are classified as young, intermediate and evolved based on the 1.3 mm and 3 mm fluxes, as well as the free-free emission at the H41α frequency (Motte et al., 2022). This classification takes into account the extent of dense gas impacted by the H II regions (Motte et al., 2022).

The 1.3 and 3 mm continuum images provides the possibility of detecting and analyzing cores and their key parameters such as temperature, molecular composition, masses, etc (Pouteau et al., 2022; Brouillet et al., 2022; Nony et al., 2023; Pouteau et al., 2023, Louvet et al. submitted). These studies demonstrated that cores are determined and characterized by the cloud formation process, their evolutionary stage, and the history of stellar formation. Additionally, they show that cores increase their masses during the protostellar phase through infalling material, with massive cores exhibiting greater mass increments than their lower mass counterparts. Simultaneously, spectral lines enable us to analyze core kinematics via DCN (Cunningham et al., 2023), demonstrating that DCN can

[1] https://www.almaimf.com/

trace different morphologies and complex velocity structures. These structures are more extended and filamentary in evolved regions compared to intermediate and young, where the DCN emission appears more compact. The N_2H^+ spectral line allows us to analyze the kinematics of the dense and cold gas (Stutz et al. in prep; Álvarez-Gutiérrez et al. in prep; Salinas et al. in prep). Additionally, SiO analysis facilitates cataloging SiO outflows in protoclusters (Towner et al., 2023), revealing that outflow properties are correlated with the total core mass and relations between outflow mass and the total mass of the protocluster.

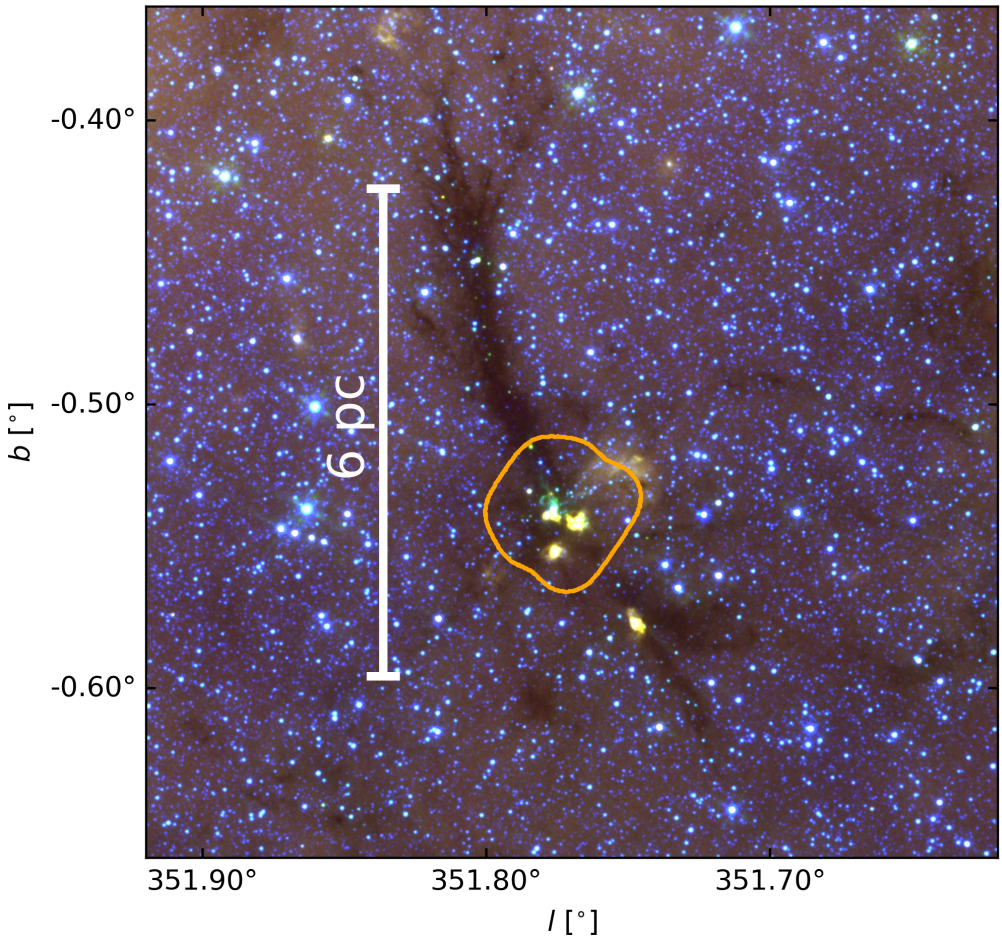

Figure 1.0.1: G351.77-0.53 filamentary region composite for IRAC bands, where the 8.0, 5.6 and 3.6 μm are shown in red, green and blue, respectively. The orange contour shows the coverage of the ALMA-IMF Large Program band 3 observation.

Filamentary structures are present in several star-forming regions throughout the Galaxy. They have been shown to hold significant importance in both low and high mass star formation processes, presenting diverse and intricate scenarios (Motte et al., 2018; Bally et al., 1987; Hacar et al., 2023; Stutz and Gould, 2016; Stutz

et al., 2018). Their formation can be triggered by different processes in which they are involved, such as front shocks induced by cloud collision or feedback, magnetic fields, gravitational instabilities and global environments (Hacar et al., 2023; Bonne et al., 2020; Issac et al., 2020; Montillaud et al., 2019; Kong et al., 2022; Stutz and Gould, 2016). Recent kinematic studies have revealed intriguingly complex scenarios within filamentary structures, encompassing fragmentation, rotation, infall, slinghshots, and more (Hacar et al., 2023; Stutz and Gould, 2016; Stutz et al., 2018; Henshaw et al., 2014; González Lobos and Stutz, 2019; Álvarez-Gutiérrez et al., 2021; Liu et al., 2019; Zhou et al., 2022). Meanwhile, a strong link has been established between filamentary structures, dense cores and protoclusters (Stutz et al., 2018; Stutz and Gould, 2016). This has led to the discovery of relations between kinematics and chemistry of dense cores and the gas surrounding the filamentary structure (Stutz and Gould, 2016; André et al., 2019; Anirudh et al., 2023; Hacar and Tafalla, 2011; Liu et al., 2020; Kim et al., 2022a; Tafalla and Hacar, 2014). Understanding the kinematic processes within filamentary structures, which are crucial to characterize the significant physical mechanisms associated with the star formation within them. This allows us to link mass, density, velocity gradients, etc, with the properties of the cores commonly found in these regions.

An important analysis that can be applied to the velocity structure are Position-Velocity diagrams (PV-diagrams), utilizing integrated intensity, velocities and positions (González Lobos and Stutz, 2019; Álvarez-Gutiérrez et al., 2021). These diagrams enable the characterization of important patterns that can provide insight into rotation, infall or cloud-cloud collision (Henshaw et al., 2014; Tobin et al., 2012; Álvarez-Gutiérrez et al., 2021; Bonne et al., 2020; Montillaud et al., 2019). Additionally, PV-diagrams allows us to characterize velocity gradients, measuring timescales, and mass inflow rates.

The fragmentation of the molecular clouds leads to the formation of clumps. Regions where gas and dust are densely concentrated, eventually giving rise to stellar cores where stars will later form (Lada and Lada, 2003). These regions, where the gas is actively turning to young stars, are termed protocluster, representing the previous phase of the stellar clusters. These structures offer valuable insights into the initial stages of star formation within clusters, enabling us to trace the evolution of the cluster and characterize the processes inherent in

the stellar formation (Lee and Hennebelle, 2016; Peretto and Fuller, 2009).

Given the emergent nature of protoclusters within the star formation process, a precise tracer becomes crucial to delineate and comprehend the intricate gas dynamics during these foundational phases, characterized by dense and freeze gas conditions. The N_2H^+(1-0) transition produces emission at $\sim$ 93 GHz. Deeper research in nearby star-forming regions has revealed emissions at seven different frequencies (Caselli et al., 1995; Thaddeus and Turner, 1975; Green et al., 1974; Turner, 1974), resulting in seven hyperfine structures in its spectra. N_2H^+ has critical densities between $\sim 6.1 \times 10^4$ cm^{-3} and 2.0×10^4 cm^{-3} at kinetic temperatures from 10 to 100 K (Shirley, 2015). N_2H^+ is formed during the gas-phase reactions from $H_3^+ + N_2 = N_2H^+ + H_2$ at temperatures lower than 20 K (Bergin et al., 2001; Yu et al., 2018; van 't Hoff et al., 2017; Jørgensen et al., 2004) and is resistant to freezing onto dust grains. However, at temperatures above 20 K, it can be destroyed by CO molecules, which are defrosted from the dust grains, leading to reactions such as $N_2H^+ + CO = HCO^+ + N_2$, or it can be destroyed by free electrons in H II regions, resulting in reactions like $N_2H^+ + e^- = N_2 + H$ or HN + N (Jørgensen et al., 2004; Tobin et al., 2013; van 't Hoff et al., 2017). These characteristics make N_2H^+ a reliable tracer for dense and cold gas. It allows us to investigate the initial stages in star-forming regions and understand the chemistry, kinematics, and dynamics in filamentary structures, protoclusters and cores (Daniel et al., 2005; Busquet et al., 2011; Schwarz et al., 2019; Fontani et al., 2006; González Lobos and Stutz, 2019; Álvarez-Gutiérrez et al., 2021).

The high-mass star-forming region G351.77-0.53 (IRAS 17233-3606) is a filamentary mid-infrared dark cloud (IRDC) (see Fig. 1.0.1) located at $\sim$ 2 $\pm$ 0.14 kpc (Reyes-Reyes et al., 2024). Recent observations, coupled with tracers analyses such as CO, HCO^+, CH_3OH, CH_3CN, SiO, ^{13}CO, $C^{17}O$, $C^{18}O$, H_2O and H_2, have shown a variety of physical processes along the filament. These processes encompass fragmentation into different clumps and the generation of turbulences, attributed to ongoing star formation activities within the region, magnetic fields and gravitational effects produced by the high-mass star formation (Sabatini et al., 2019; Yu et al., 2018; Leurini et al., 2019, 2011a). Focusing in the most prominent clump (G351.77 hence), clear signs of bipolar outflows has been discovered at very high velocities with young kinetics effects (Zapata et al., 2008; Leurini et al., 2014, 2013, 2011b, 2008a,b; Klaassen et al., 2015; Antyufeyev et al., 2016). These

outflows are closely linked to Young Stellar Objects (YSOs). Additionally, an evident gradient is observed in several tracers, revealing two different velocity components (Leurini et al., 2019). Furthermore, the analysis of the observations at scales $<$ 1kAU, reveal the existence of disks with signals of outflows, infall and rotation (Zapata et al., 2008; Beuther et al., 2017).

In this paper, we focus on the kinematics of the dense gas within the massive G351.77 protocluster, analyzing the N_2H^+ (1-0) spectral line, which serves as a tracer for dense and cold gas, as mentioned previously. To achieve this, we will process and combine the observations obtained form the 7m-array and 12m-array configurations within ALMA-IMF Large Program, feathering them with TP observations. We will utilize specialized software to fit the data. We plain to make use of the PV-diagrams to characterize structures and comprehend the physical process occurring inside the protocluster. We aim to identify patterns that can provide insights into different motions probed by the radial velocity in the dense gas.

Chapter 2

Data

We have obtained access to the N_2H^+ (1-0) observations of G351.77 massive protocluster in the 3 mm spectral band, observed by the 12m-array, 7m-array and TP configurations obtained from the ALMA-IMF Large Program (Motte et al., 2022). Our data has an spatial resolution of $\sim$ 1540 AU and a spectral resolution of 0.23 km/s. The beam sizes are (2.3" $\times$ 2.07"), (16.9" $\times$ 10.1") and (69.6" $\times$ 69.6") for 12m-array, 7m-array, and TP respectively. In our analysis, we have used the core catalog (Louvet et al. submitted) derived from the continuum images of the 1.3 mm band (Ginsburg et al., 2022a) and the core kinematics obtained from DCN (3-2) spectral line fits (Cunningham et al., 2023). Additionally we are using H_2 column density map of G351.77 derived of a combination of 1.3 mm band, SOFIA/HAWC+ (53 μm, 89 μm, and 214 μm), APEX/SABOCA (350 μm) and APEX/LABOCA (870 μm) observations (Dell'Ova et al. submitted)

2.1 N_2H^+ data reduction

The data reduction process was performed using CASA 6.2 along with the ALMA-IMF data pipeline[1]. Initially, we started with the reduction of the 12m-array data to determinate the optimal parameters settings to achieving the highest quality results. Among the different parameters tested in *tclean*[2] CASA task, the following were investigated: *niter*, *threshold*, *deconvolver*, *pbmask*, *pblimit* and *scales*. These parameter values were selected based on the analysis of the residual,

[1] https://github.com/ALMA-IMF/reduction
[2] https://casadocs.readthedocs.io/en/stable/api/tt/casatasks.imaging.tclean.html

model, and image returned after each reduction process. Subsequently, we applied the same parameter values to combine the 12m-array and 7m-array data with *tclean* to increase the Fourier coverage (7M12M, henceforth). However, in order to improve the result of this combination it was necessary to change a few values for some parameters.

Continuum subtracted was accomplished using the CASA task *imcontsuv*[3]. This task involves the channels containing free line emission to generate a continuum model, which is subtracted from the line emission channels. This process yields the continuum subtracted 7M12M data.

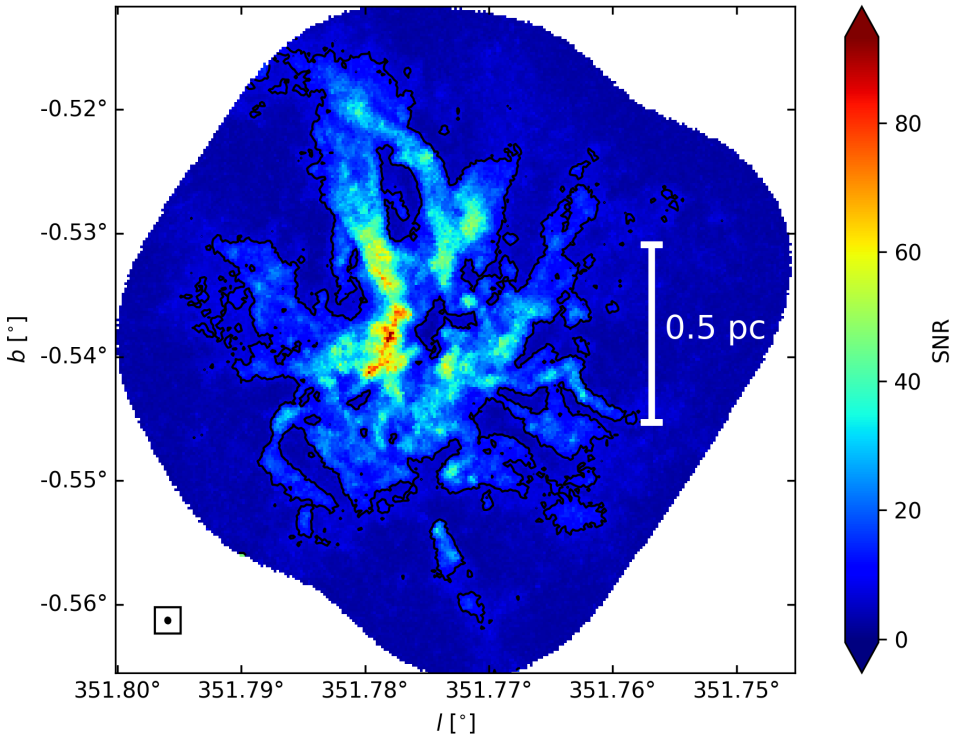

Figure 2.1.1: SNR map of the N_2H^+ (1-0) line in the G351.77 protocluster. Spectra with high SNR are distributed following filamentary structures. The black contour shows the spectra with SNR > 9. The ellipse in the bottom-left corner represent the beam size of the N_2H^+ data.

As a final step, we employed the CASA task *feather*[4] to feather the 7M12M continuum subtracted data with TP, with the purpose of reconstructing the extended emission of N_2H^+ line. Here we define 7M12M continuum subtracted as the high resolution data and TP as the low resolution data. Finally obtaining a

[3] https://casadocs.readthedocs.io/en/stable/api/tt/casatasks.analysis.imcontsub.html
[4] https://casadocs.readthedocs.io/en/stable/api/tt/casatasks.imaging.feather.html

fully combined image (original data forward), ensuring consistency in intensities without random peak divergences. This resulted in a broad Signal to Noise Ratio (SNR) range and well defined structures with a favorable SNR (see Fig. 2.1.1).

Chapter 3

Line fitting process

Since our main goal in this paper is to analyze the fine and large scale protocluster kinematics of the dense gas, we require the use spectral line fitting to pull out the velocity field. Moreover, the spectra line fitting of N_2H^+ provides additional parameters of interest, i.e. the optical depth (τ) and excitation temperatures (T_{ex}, see below). The first examination of the spectral cube immediately reveals that multiple velocity components exist over a significant number of spectra (see Fig. B.0.4). Hence, we adopt an iterative approach to the line fitting, described in detail below.

In brief, we only fit spectra with SNR > 9. This approach stems out from our experimental findings, which reveal that spectra with a SNR < 9 are inadequately fitted, whose uncertainties increase as well (see Fig. 2.1.1 and § Appendix A). We ultimately fit the spectral cube with 2-velocity components when possible (driven mainly by signal-to-noise considerations, see below), and 1-component when the spectra are either relatively simple, or the noise precludes more detailed velocity decomposition. To accomplish this fitting, we begging with a 1-velocity-component fit and a 2-velocity-component fit, which are independent. We call these two relatively "raw" fits the First Fitting Procedures (FFPs). We then analyze the signal-to-noise of the decomposed spectra to identify where we have reliable 2-velocity-component fits; where we do not, we adopt the 1-velocity-component fit for the spectrum being analyzed (see Fig. 3.0.1).

Throughout, we use the N_2H^+ model *n2hp_vtau*[1] from PySpecKit[2] (Ginsburg et al., 2022b; Ginsburg and Mirocha, 2011) to fit the cube (e.g. Álvarez-Gutiérrez et al., 2021; González Lobos and Stutz, 2019; Redaelli et al., 2019). This procedure returns 4 parameters per velocity component: excitation temperature (T_{ex}), optical depth (τ), centroid velocity (v), and line width ($\sigma(V)$). To fit these, four different guesses must be entered to initialize PySpecKit. Moreover, in addition to the guesses, each parameter is assigned both a lower and upper limit value, defining the range within which the final fitted values will lie. In Table 3.0.1 we show the guess and limit values for each parameter used in the FFP and in the final fit. After the fitting process PySpecKit returns the model spectra, parameter values (see above) and associated parameter errors. See Fig. 3.2.1 and Fig. 3.2.2 for example maps of the spectral fits, specifically the integrated intensity and the line width. Finally, we must merge the 1- and 2-velocity-component fits into one model cube, as described below (see Fig. 3.4.1). In the text that follows we present more details on the procedures outlined above.

Table 3.0.1: Guess and limit values entered for 1- and 2-velocity-component fits.

Parameters	T_{ex} [K]	τ	v [km/s]	σ_V [km/s]	T_{ex} [K]	τ	v [km/s]	σ_V [km/s]
	Single velocity component							
FFP guesses	20.0	1.0	-3.0	1.0				
Final guesses	12.4	3.64	-3.77	1.0				
Limits	(2.73, 100)	(0, 100)	(-13, 3)	(0, 6)				
	First-velocity-component				Second-velocity-component			
FFP guesses	20.0	1.0	-5.0	1.0	20.0	1.0	-2.0	1.0
Final guesses	9.22	4.60	-5.0	0.83	9.0	7.4	-2.6	0.66
Limits	(2.73, 100)	(0, 100)	(-13, 3)	(0, 6)	(2.73, 100)	(0, 100)	(-13, 3)	(0, 6)

3.1 One-velocity-component fit

As an initial step, we employed a straightforward approach by fitting a 1-velocity-component across the entire spectral cube entering the "FPP guesses" and "Limits" listed in Table 3.0.1. Since our goal is to achieve the best fit possible, we can utilize the parameters returned by the FFP to refine the entered guesses and then, use them in a new fitting process. Thus we give to PySpecKit values that are more representative of the data in order to improve the modeled cube and parameters returned. We derive these new guesses measuring the average of each

[1] https://pyspeckit.readthedocs.io/en/latest/example_n2hp_cube.html
[2] https://pyspeckit.readthedocs.io/en/latest/index.html#

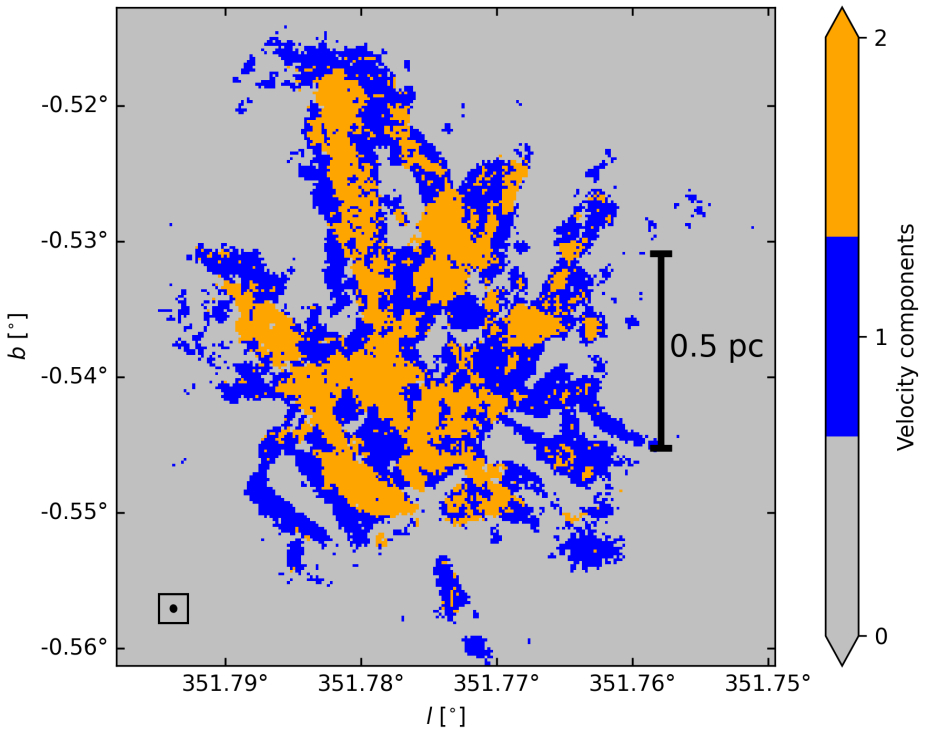

Figure 3.0.1: Map of velocity component of N_2H^+ in G351.77 protocluster. The blue pixels represent the spectra maintained with a 1-velocity component fit (59%), while the orange pixels represent the spectra maintained with a 2-velocity-component fit (41%) after applying the criteria explained in § 3.3. Most of the orange pixels are located in central regions, where we observe the highest SNR and integrated intensity values. While the blue ones are located mostly in the borders. The ellipse in the bottom-left corner represent the beam size of the N_2H^+ data.

parameter (see "Final guesses" in Table 3.0.1), which are used to produce the final model with 1-velocity-component fit.

However, the FFP reveals an issue produced by spectra with $\tau < 1$, which generate misleading estimations of T_{ex}, whose values lie between 80 K $\lesssim T_{ex} < 10^4$ K (this issue also occurs in 2-velocity-component fit process). Due the methodology used by PySpecKit to estimate T_{ex}, low values of τ increases the uncertainties, making difficult to estimate T_{ex} correctly. Since we expect to keep the most of data and use reliable values of each parameter, we fix this issue re-fitting the spectra with $\tau < 1$, assigning them a constant T_{ex} value (e.g. Caselli et al., 2002a,b).

The spectra with $\tau < 1$ are selected and separated from the cube to be re-fitted by 1-velocity-component with a constant T_{ex} value, whose value comes from averaging

T_{ex} of spectra with $\tau > 1$. The re-fitted spectra use the "Final guesses" listed in Table 3.0.1). However, the T_{ex} limits will be now (2.73 K, 12.4 K).

At the end of this process, we obtain two separated spectral model and parameters fitted by 1-velocity-component. From the spectra with $\tau > 1$, and from spectra with $\tau < 1$. As a final step in this process, we merge these two spectral models and parameters, creating a final spectral model entirely fitted by 1-velocity-component, with its parameters and associated errors.

3.2 Two-velocity-component fit

Upon examining the spectral cube, we noted the presence of two distinct velocity components in several spectra. Consequently, a 1-velocity-component fit is not enough to describe the kinematics of the data. This force us to fit two-velocity-components in the spectral cube, entering the "FFP guesses" and "Limits" for each velocity component, listed in Table 3.0.1. In a similar way as we made in § 3.1 and in order to get the best fit, we derive new guesses measuring the average of the values returned for each parameter of each component (see "Final guesses" in Table 3.0.1). These new guesses are used to generate the final model with 2-velocity-components fit.

As we mentioned in § 3.1, spectra with $\tau < 1$ produce bad estimations of the T_{ex}. Therefore, spectra with $\tau < 1$ is selected and separated to be re-fitted. However, due we are fitting two-velocity-components, it is necessary to separate the spectra in 3 different conditions (see Table 3.2.1), to assigning them a constant T_{ex} value. These constant values come from averaging T_{ex} of spectra with $\tau > 1$ of each component. The re-fitted spectra will use the same "Final guesses" listed in Table 3.0.1, while the T_{ex} limits depend of the condition (see Table 3.2.1).

Table 3.2.1: New T_{ex} limits applied for each different condition for the 2-velocity-component fit based on τ values.

Number	Condition	$T_{ex,1}$ [K]	$T_{ex,2}$ [K]
1	$\tau_1 < 1$ & $\tau_2 \geq 1$	(2.73, 9.22)	(2.73, 100)
2	$\tau_1 \geq 1$ & $\tau_2 < 1$	(2.73, 100)	(2.73, 9.0)
3	$\tau_1 < 1$ & $\tau_2 < 1$.	(2.73, 9.22)	(2.73, 9.0)

The re-fitted process produce in some spectra a new τ estimation, whose values can be < 1. As we already know, this generate a bad estimation of T_{ex}. Specifically,

this occurs applying the condition number 1 and number 2. It is necessary to select and separate the re-fitted model spectra in two new conditions:

a. The model returned from the condition number 1 with $\tau_2 < 1$.

b. The model returned from the condition number 2 with $\tau_1 < 1$.

These spectra are re-fitted again, using the "Final guesses" and "Limits" of the Table 3.0.1. However, the T_{ex} limits are now T_{ex} = (2.73 K, 9.22 K) for the condition "a", and T_{ex} = (2.73 K, 9.0 K) for the condition "b".

The separation of the cube in different conditions to re-fit the spectra with $\tau < 1$, provide us the security of all spectra have the greater freedom in order to estimate τ values and obtain good or more reliable T_{ex} values in each spectra.

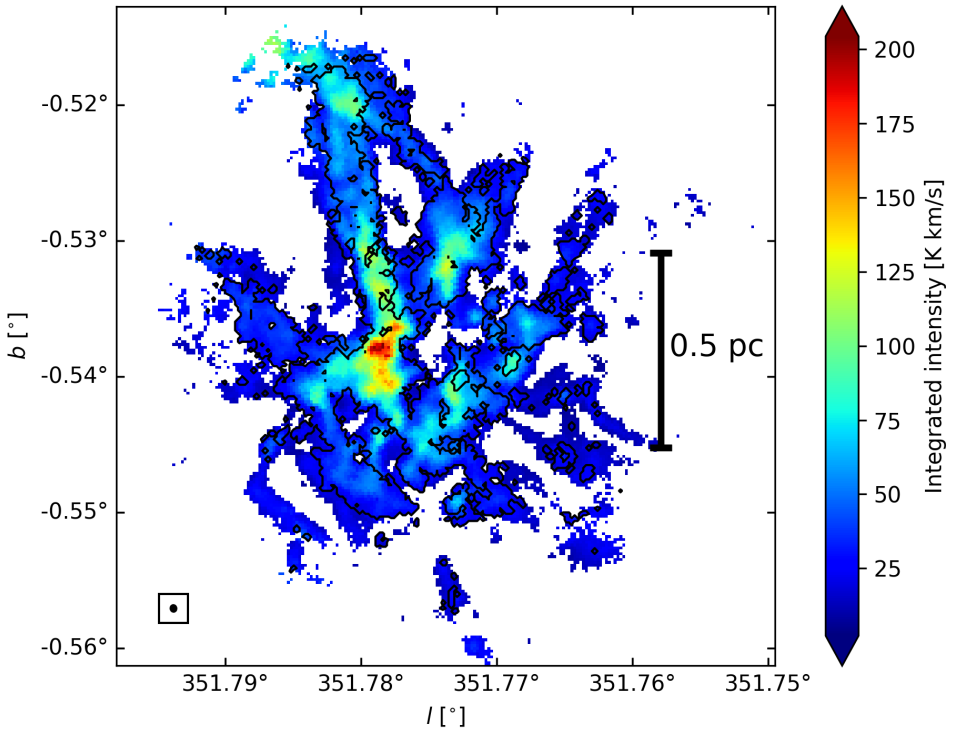

Figure 3.2.1: Integrated intensity map from the spectral model of G351.77. The spectra inside the black contour are fitted by 2-velocity-components. The ellipse in the bottom-left corner represents the beam size of N_2H^+ data.

At the end of this process, we obtain 6 separated model spectra and parameter cubes fitted by 2-velocity-components. As a final step in this process, we merge these 6 spectral models and parameter cubes, creating a final spectral model entirely fitted by 2-velocity-components, which components we will refer to

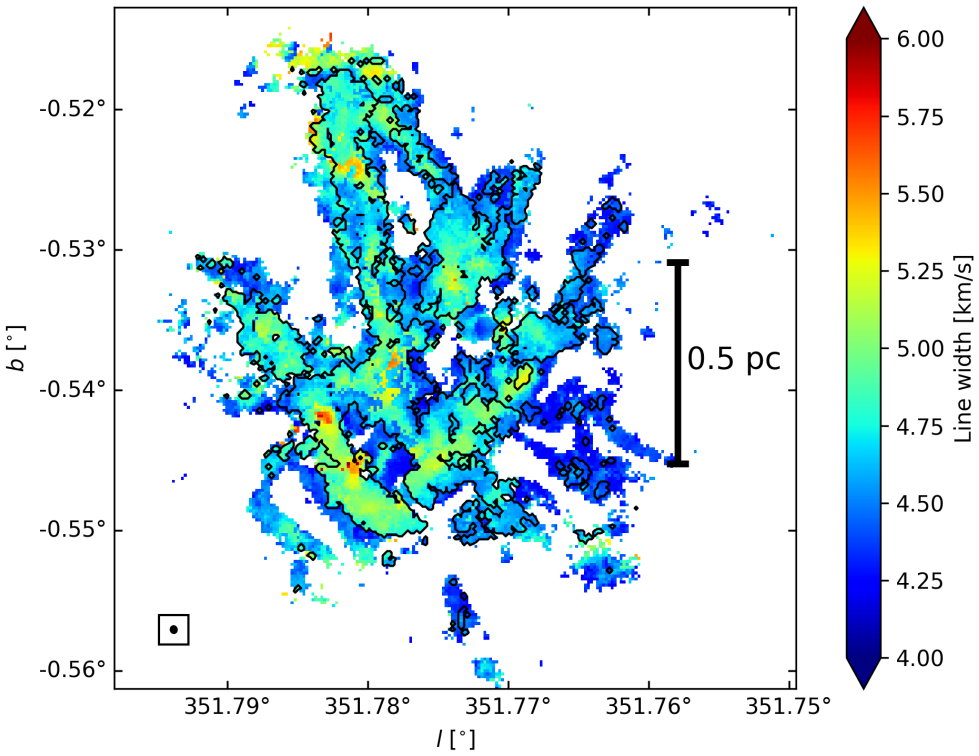

Figure 3.2.2: Line width map from the spectral model of G351.77. The spectra inside the black contour are fitted by 2-velocity-components. The ellipse in the bottom-left corner represents the beam size of N_2H^+ data.

as the "First-velocity-component", and the "Second-velocity-component", with their centroid velocities being the lowest and highest, respectively, and with its parameters and associated errors.

3.3 Best fit and merging models

In the § 3.1 and § 3.2 we showed the complete fitting process of the data, fitting the whole cube with 1- and 2-velocity-components. However, our spectral cube shows spectra where we can identify just 1-velocity-component (see Fig. B.0.3), spectra where we can identify 2-velocity-components (see Fig. B.0.4), and spectra where it is not possible to make a clear identification by eye. Furthermore, it is necessary to determine what fit (1- or 2-velocity-components) is better of each spectra to simplify our analysis and to keep reliable kinematic information of the protocluster, avoiding to add a velocity component where it does not really exist or vice-versa. Thus, we devised a method to know if 1- or 2-velocity-components fit is better for each spectra based on a signal-to-noise criteria, and the parameters

associated to each spectra, specifically, the line width.

In order to determine if the spectra is better fitted by 1- or 2-velocity-components we:

1. Check the $\sigma(V)$ value in the spectral model fitted by 2-velocity-components. In a quick inspection of the spectral model fitted by 2-velocity-components, we observe some spectra that look like flats, that is, without emission, and whose $\sigma(V)$ is equal to 0 (see Fig. B.0.1). Which implies that if $\sigma(V)$ is 0 in the First- or the Second-velocity-component, one of the two modeled velocity components is not real, and we are artificially forcing the fit a second velocity component. All spectra with this characteristic is maintained with the 1-velocity-component fit (see Fig. B.0.1).

2. Measure the SNR of the velocity component with lower intensity for each spectra in the spectral model fitted by 2-velocity-components. Deeper inspection shows that some additional velocity components have a peak intensity lower or similar to noise value. In other words, we are fitting noise. So, if the peak intensity is lower than 5 times the noise measured in that spectra from the original cube, the 1-velocity-component fit is adopted. Then, we ensure the reliability of the additional velocity component (see Fig. B.0.2).

After of applying these 2 criteria, we obtain spectra fitted by 1-velocity-component (see Fig. B.0.3), and spectra fitted by 2-velocity-components (see Fig. B.0.4). All these spectra are merged in order to create a final spectral model with spectra with 1- and 2-velocity components in it (see Fig. 3.0.1). It is possible to observe that most of the spectra fitted by 2-velocity-components are located in internal regions with high integrated intensity (see Fig. 3.2.1).

3.4 Bluest and Reddest velocity component

From the four parameters given by PySpecKit of N_2H^+ spectra, the centroid velocity is the one that have the lowest uncertainties, and which give us information about the velocity of the region where we observe the emission. The centroid velocity map in Fig. 3.4.2 shows a clear large-scale velocity gradient (VG) that looks perpendicular to the b coordinate axis and to the direction in which the

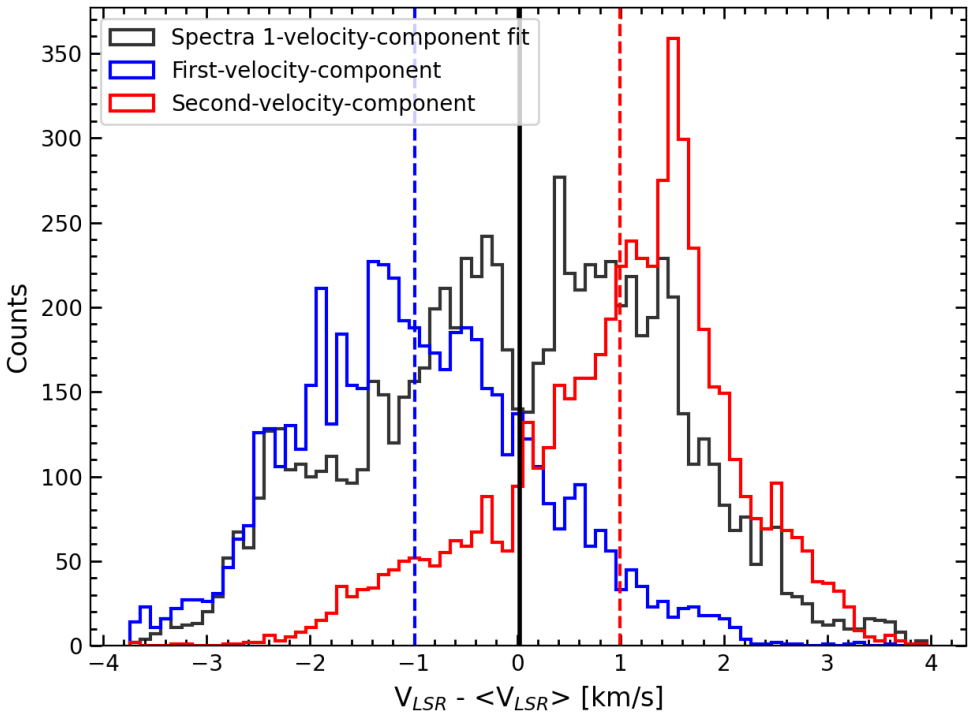

Figure 3.4.1: The black histogram represent the centroid velocity distribution of the spectra fitted by 1-velocity-component. The blue and red histogram shows the centroid velocity distribution of the First- and the Second-velocity-component, respectively. The black solid line represent the middle point $X = 0.255$ km/s measured from the (Eq. 3.4.1), which is used to divide the black histogram in 2 parts, as we explained in § 3.4. The centroid velocity distribution of the 1-velocity-component fit to the left of the black solid line, and the blue histogram, are the Blues component. While the centroid velocity distribution of the 1-velocity-component fit to the right of the black solid line, and the red histogram, are the Reddest component. The dashed blue and red lines represent the average of centroid velocity of the blue and red histograms, respectively.

molecular cloud that hosts the protocluster extends (Mother filament). On the other hand, we observe big differences between the velocities of the spectra with 1- and 2-velocity-components (see Fig. 3.4.2). This occurs because the velocity measured for the spectra with 2-velocity-components represent the averaged centroid velocity between the First-velocity-component and the Second-velocity-component in the spectra. In order to avoid this difference and clarify the analysis, it is necessary to separate the spectra fitted by 1-velocity-component and set them as part of the First-velocity-component or the Second-velocity-component. To achieve this, we define a velocity limit as a middle point based on the velocity distributions of the First-velocity-component and the Second-velocity-component

(see Fig. 3.4.1).

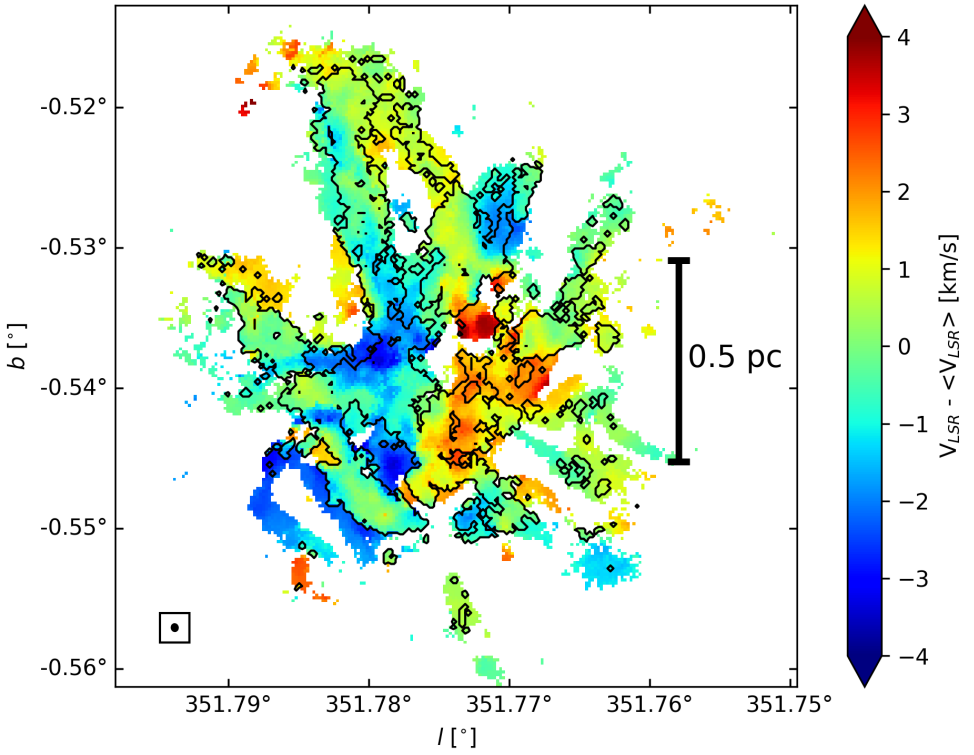

Figure 3.4.2: Centroid velocity map from the spectral model of G351.77. The spectra inside the black contour are fitted by 2-velocity-components. The ellipse in the bottom-left corner represents the beam size of N_2H^+ data.

To measure the velocity limit to divide the 1-velocity-component, we apply the following relation:

$$< v_1 > + X \times \sigma_1(V) = < v_2 > - X \times \sigma_2(V) \tag{3.4.1}$$

where $< v_1 >$ is the average velocity of the First-velocity-component, $\sigma_1(V)$ is the standard deviation of the First-velocity-component, $< v_2 >$ the average velocity of the Second-velocity-component, $\sigma_2(V)$ is the standard deviation of the Second-velocity-component, and X is the velocity limit to use as middle point. Applying the Eq. 3.4.1 we obtain a $X = 0.255$ km/s. This value allow us to separate the velocity distribution of the 1-velocity-component fit into two parts, and combine them with the First- and the Second-velocity-component. We define as "Bluest component" to the merger of the First-velocity-component, and the spectra from 1-velocity-component fit with centroid velocity < 0.255 km/s, while that we define as "Reddest component" to the merger of the Second-velocity-component, and

the spectra from 1-velocity-component fit with centroid velocity > 0.255 km/s, deriving 2 centroid velocity maps (see Fig. 3.4.3 and Fig. 3.4.4).

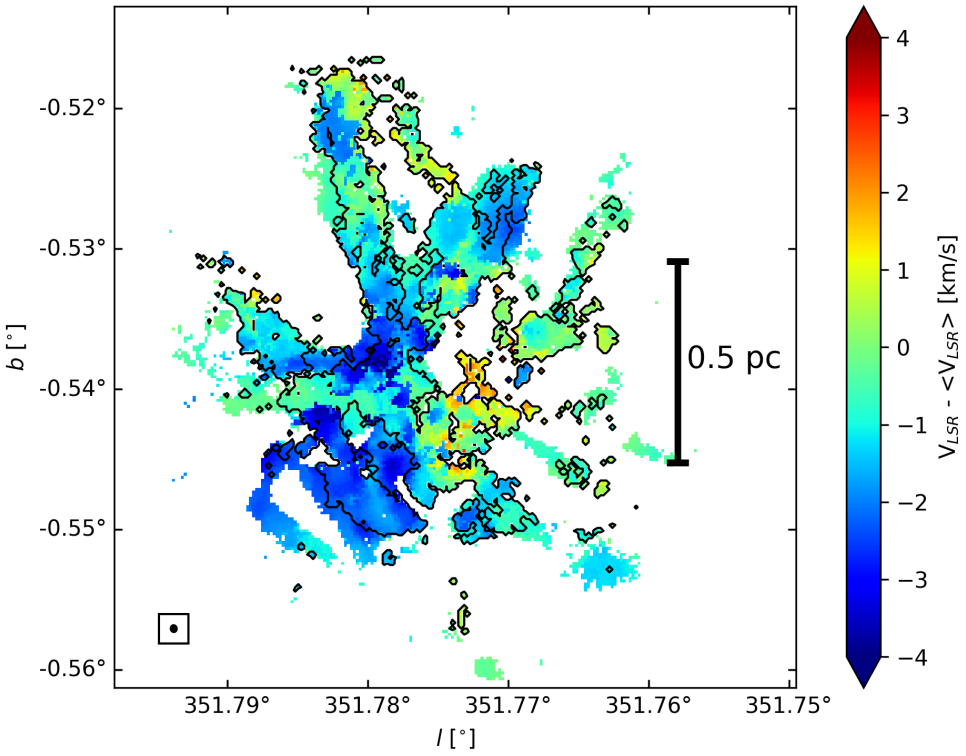

Figure 3.4.3: Bluest component derived from the spectral model fitted by 1- and 2-velocity components. The spectra inside the black contour are fitted by 2-velocity-components. The ellipse in the bottom-left corner represents the beam size of N_2H^+ data.

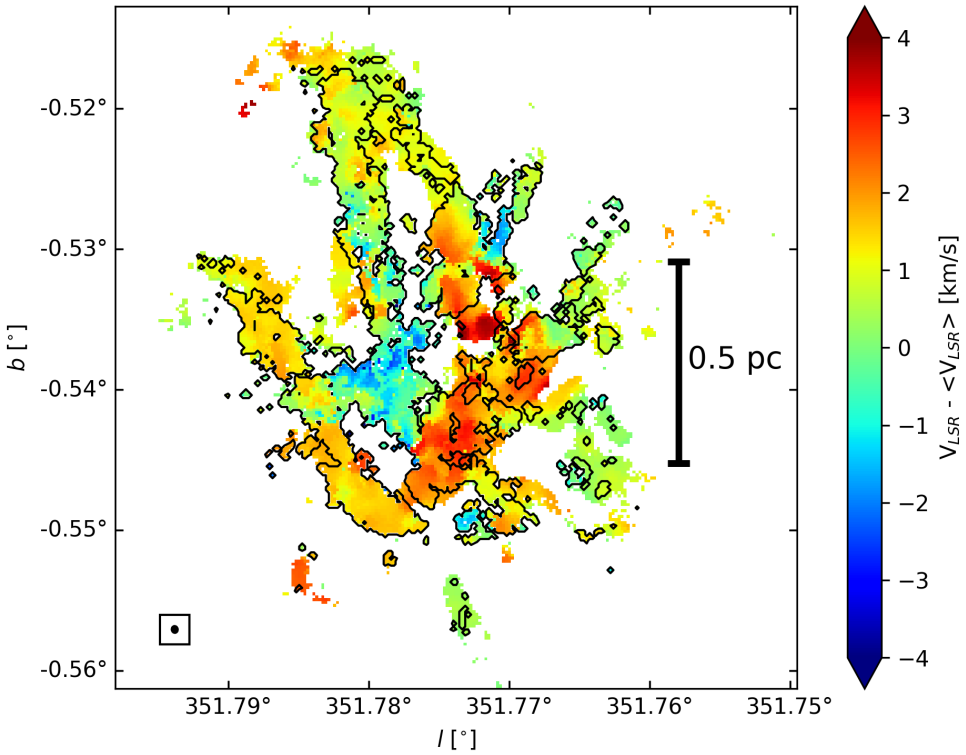

Figure 3.4.4: Reddest component derived from the spectral model fitted by 1- and 2-velocity-component. The spectra inside the black contour are fitted by 2-velocity-components. The ellipse in the bottom-left corner represents the beam size of N_2H^+ data.

Chapter 4

Column Density and masses

The spectral line fitting of N_2H^+ shown in § 3 provides relevant information about the N_2H^+ spectra, specifically excitation temperature (T_{ex}), optical depth (τ), and line width (σ(V)). These parameters enable the estimation of column density maps of N_2H^+ ($N(N_2H^+)$) (see Fig. 4.0.1 and Eq. 4.1.1) and the mass of N_2H^+ ($M(N_2H^+)$) (see Eq. 4.1.2) in the protocluster zone, which can be calculated for both the Bluest component and the Reddest component (see below). Additionally, the column density map of H_2 ($N(H_2)$) provided by Dell'Ova et al. submitted (see Fig. 4.2.1), give us the opportunity of estimate the N_2H^+ relative abundances ($X(N_2H^+)$) in the protocluster (see Fig. 4.2.2) and over nine 1.3 mm band cores from the core catalog of Louvet et al. submitted (see Table 4.1.1). Given the lower resolution of the $N(H_2)$ data, it is necessary to reduce the resolution of N_2H^+ raw data at the same resolution of $N(H_2)$ and re-scale it to the same pixel size of $N(H_2)$ (see Fig. 4.2.3). Subsequently, is implemented the reduction and fitting process shown in § 2.1 and § 3, respectively. In this way, it is feasible to analyze and to work with both data at the same time without discrepancies in order to estimate the $X(N_2H^+)$ correctly. However, taking into account the significant scatter of $X(N_2H^+)$, have been implemented two different methods to maintain the most representative value of the protocluster (see below). On the other hand, the $X(N_2H^+)$ derived from the Eq. 4.2.1 is used to re-estimate the $N(H_2)$ at a higher resolution, derived from the N_2H^+ emission. This facilities the measurement of mass of H_2 ($M(H_2)$) at smaller scales, allowing to estimate H_2 masses related to cores and velocity gradients (see § 5).

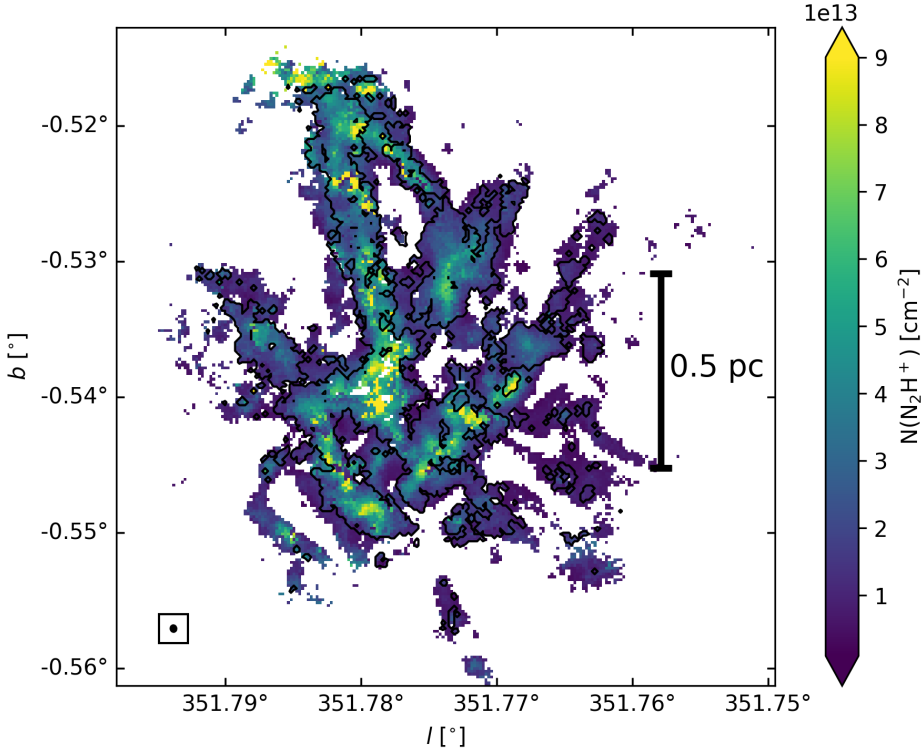

Figure 4.0.1: N_2H^+ column density map in the G351.77 protocluster derived from Eq. 4.1.1. The black contours shows the spectra with two velocity components. The ellipse in the bottom-left corner represent the beam size of N_2H^+ data.

4.1 N_2H^+ column density and mass

In order to estimate the column density of N_2H^+ we are employing the following expression (Redaelli et al., 2019; Caselli et al., 2002b):

$$\mathrm{N}(\mathrm{N_2H^+}) = \frac{4\pi^{3/2}}{\sqrt{\ln(2)}} \frac{\nu^3 \cdot Q \cdot \sigma(V)}{c^3 \cdot A_{ul} \cdot g_u} \frac{\tau}{e^{h\nu/k_b T_{ex}} - 1} \cdot e^{E_u/k_b T_{ex}} \tag{4.1.1}$$

where $\sigma(V)$, τ and T_{ex} correspond to the parameters returned by our fits, while ν is the frequency, Q is the partition function, c is the speed of light, A_{ul} is the Einstein coefficient, g_u is the statistical weight, h is the Planck's constant, k_B is the Boltzmann's constant and E_u is the energy of the upper limit (Redaelli et al., 2019; Mangum and Shirley, 2017; Pagani et al., 2008). We apply this expression over the Bluest component and the Reddest component to obtain the column density of each one, $\mathrm{N_1}(\mathrm{N_2H^+})$ and $\mathrm{N_2}(\mathrm{N_2H^+})$ respectively. The total column density $\mathrm{N_T}(\mathrm{N_2H^+})$ is obtained by adding both column densities (see Fig. 4.0.1

and Table 4.1.1). Then, we can measure the mass of N_2H^+ applying the following expression:

$$M(N_2H^+) = N(N_2H^+) \cdot A_{pixel} \cdot m_{N_2H^+} \tag{4.1.2}$$

where $N(N_2H^+)$ is given by the Eq. 4.1.1, A_{pixel} corresponds to the area of the pixel, and $m_{N_2H^+}$ corresponds to the mass of N_2H^+ molecule, where $m_{N_2H^+} = 4.817 \times 10^{-26}$ kg. Table 4.1.1 shows the mass for the Bluest and Reddest component, and the total N_2H^+ mass in the protocluster.

Table 4.1.1: N_2H^+ column density estimations. Where N_1, N_2 and N_T corresponds to the Bluest component, the Reddest component and N_1 + N_2, respectively.

N_{col}	$N(N_2H^+)$ $[1/cm^2]$	$M(N_2H^+)$ $[M_\odot]$
$N_1(N_2H^+)$	1.416×10^{17}	1.8×10^{-6}
$N_2(N_2H^+)$	1.755×10^{17}	2.2×10^{-6}
$N_T(N_2H^+)$	3.171×10^{17}	4.0×10^{-6}

4.2 N_2H^+ Relative abundances

Since we expect to estimate $N(H_2)$ at higher resolutions, as the provided by N_2H^+, it is necessary to know the $X(N_2H^+)$ in the protocluster, which is given by the following expression:

$$X(N_2H^+) = \frac{N(N_2H^+)}{N(H_2)} \tag{4.2.1}$$

However, the beam size of the $N(H_2)$ data is (6" × 6"), whereas the beam size of N_2H^+ is (2.3" × 2.07"). This implies that the angular resolution of N_2H^+ raw data must decrease. To achieve this, the N_2H^+ raw data is convolved, obtaining the N_2H^+ raw data whose beam size is the same as for $N(H_2)$. Then, this convolved N_2H^+ data is re-scaled at the same pixel size of $N(H_2)$. This convolved and re-scaled N_2H^+ data go through the data reduction and line fitting process described in § 2.1 and § 3, before to estimate the $X(N_2H^+)$.

With the purpose of reducing the uncertainties of $X(N_2H^+)$, we select the spectra with $N(N_2H^+)$ and $N(H_2)$ SNRs < 4. Applying the Eq. 4.2.1 on these spectra

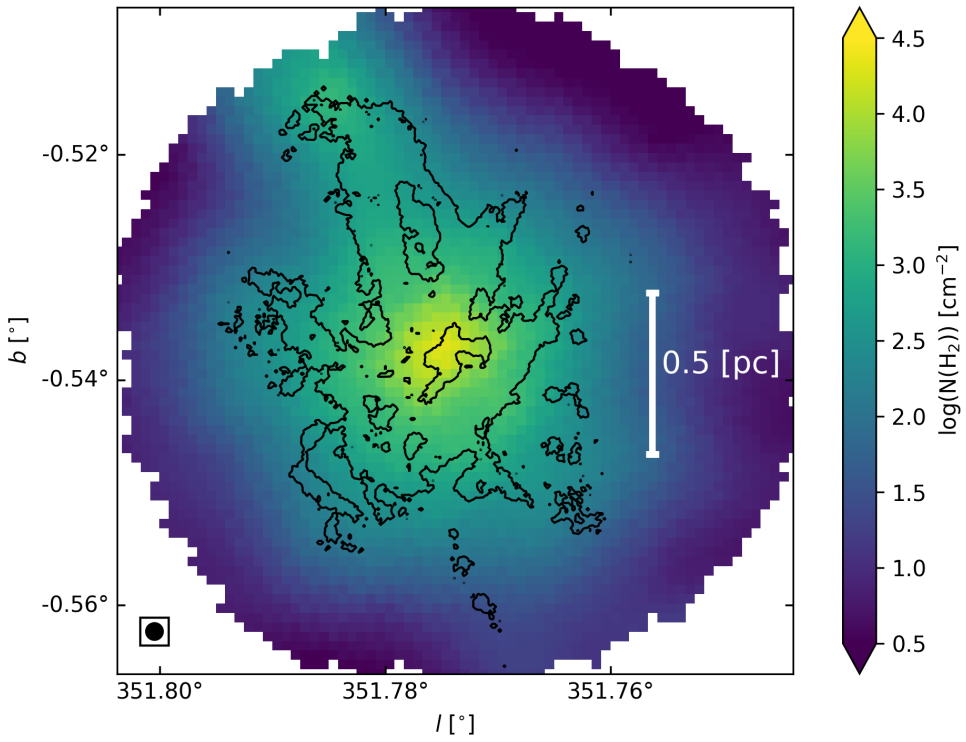

Figure 4.2.1: H_2 column density map of G351.77 protocluster . The black contour represents the spectra with $N_T(N_2H^+) > 1 \times 10^{13}$ 1/cm^2. The circle on bottom left represents the beam size of $N(H_2)$.

we obtain the relative abundance values for pixel, which appear to follow a log-normal distribution (see Fig. 4.2.2). Based on this observations, our objective is to determinate a reference value of $X(N_2H^+)$, whose value will be equal to the mode of this distribution (the mean within the peak of the histogram (see Fig. 4.2.2)). However, this value may vary depending on the bin width used. Therefore, we utilized two different methods to derive the $X(N_2H^+)$:

1. The *Freedman Diaconis Estimator* method: this function[1] from the Numpy library provides the optimal number of bins (bin width) based on the kind of the distribution, the variability, and the size of the data.

2. Measure the mean within the first, the second, and the third most prominent peaks in the histogram (the dashed black, dashed yellow, and dashed blue lines in Fig. 4.2.2, respectively). Then, taking the average of these 3 mean values across varying bin widths, until the log-normal distribution shape is lost.

[1] https://numpy.org/devdocs/reference/generated/numpy.histogram_bin_edges.html

Applying the method 1), the estimated optimal number of bins for our data distribution is 119 (see Fig. 4.2.2). With this number of bins, the mean within the most prominent peak corresponds to $X(N_2H^+) = (1.66 \pm 0.46) \times 10^{-10}$. Additionally, applying the method 2), we observe a clear convergence trend. And as the bid width decreased, the average of the means converge to $X(N_2H^+) = 1.66 \times 10^{-10}$ before losing the shape of the distribution.

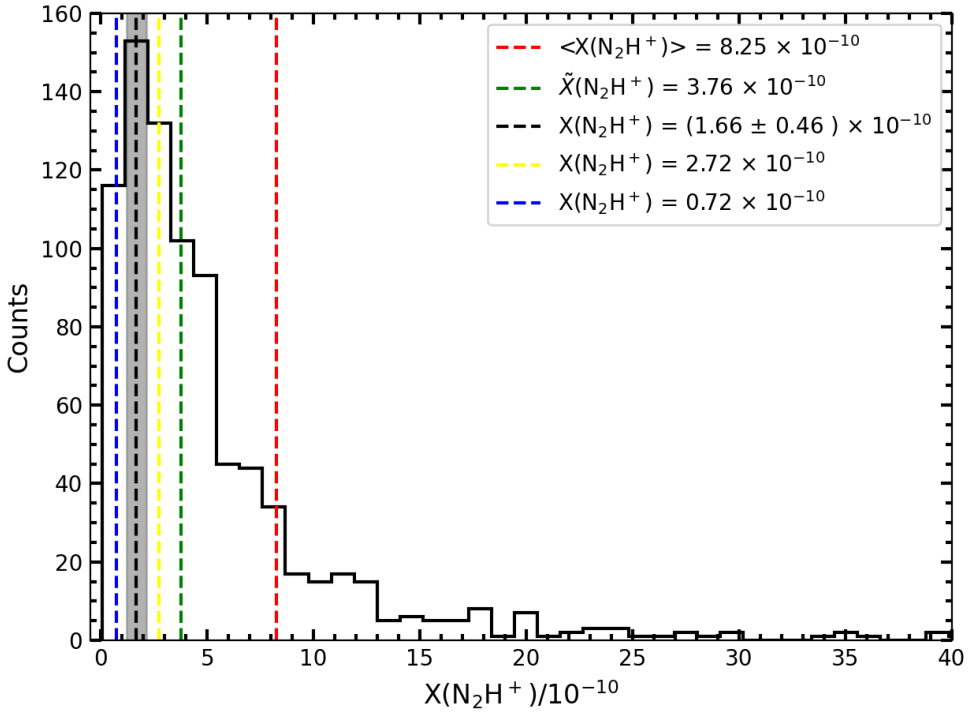

Figure 4.2.2: Distribution of $X(N_2H^+)$ in G351.77 protocluster zone. The red and green dashed lines represent the mean, and the median of the distribution, respectively. While the black dashed, yellow dashed, and blue dashed lines represent the mean inside the first, the second, and the third most prominent peaks of the distribution, respectively. The shadow region represents the size of the error around the mode.

Using these two methods, we can realize that the relative abundance is the same. Thus, we define the relative abundance of G351.77 in the protocluster zone as $X(N_2H^+) = (1.66 \pm 0.46) \times 10^{-10})$, whose value is used to determinate $N(H_2)$ at a higher resolution based on $N(N_2H^+)$, and then the $M(H_2)$ following the Eq. 4.2.2 (see Table 4.2.1).

$$M(H_2) = N(H_2) \cdot A_{pixel} \cdot m_{H_2} \tag{4.2.2}$$

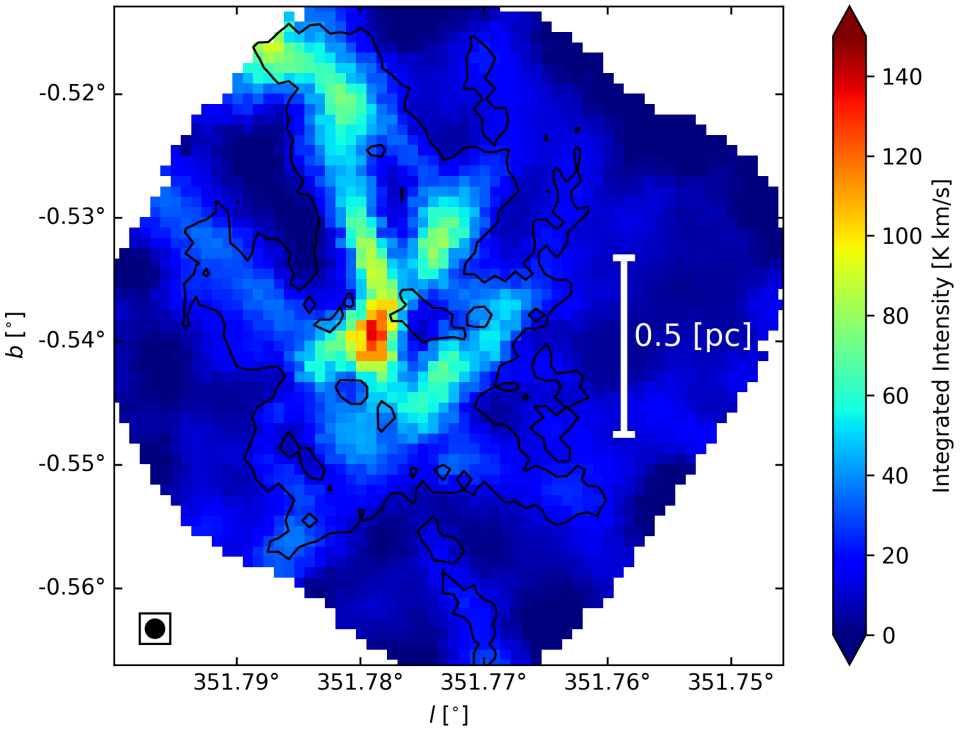

Figure 4.2.3: Integrated intensity map of the convolved and re-scaled N_2H^+ data of G351.77 protocluster to the same angular resolution and pixel size as $N(H_2)$. The black contour represents the spectra with $N(N_2H^+)$ SNR > 4. The ellipse on bottom-left represents the beam size of $N(H_2)$.

where $N(H_2)$ is the new estimation derived from $N(N_2H^+)$, A_{pixel} is the area of the pixel, and m_{H_2} the mass of the H_2 molecule, where $m_{H_2} = 3.347 \times 10^{-27}$ kg.

Table 4.2.1: H_2 column density estimations. Where N_1, N_2 and N_T corresponds to the Bluest component, the Reddest component and $N_1 + N_2$, respectively.

N_{col}	$N(H_2)$ $[1/cm^2]$	$M(H_2)$ $[M_\odot]$
$N_1(H_2)$	0.851×10^{27}	740
$N_2(H_2)$	1.054×10^{27}	917
$N_T(H_2)$	1.905×10^{27}	1658

We finally estimate a H_2 total mass in G351.77 in the protocluster zone $\sim$ 1660 $\pm$ 458 $M_\odot$, which we define as a lower mass limit for the G351.77 protocluster region, as it corresponds to the mass derived from the regions with N_2H^+ emission. Additionally, the total mass estimated directly from the H_2 column density map given by Dell'Ova et al. submitted, is $M(H_2) \sim 2820$ $M_\odot$. However, if we consider the mass inside the N_2H^+ coverage, we estimate a $M(H_2) \sim 2000$ $M_\odot$. Even if we see a $\sim$ 340 $M_\odot$ difference, it still inside of our uncertainties. We considered this

Table 4.2.2: Physical parameters given by the spectral line fitting shown in § 3 and column density estimations shown in this section, inside the 1.3 mm core regions. The numbers in the "Core" column represent the number of the cores of Table E.11 in Louvet et al. submitted, and Table F.9 in Cunningham et al. (2023).

n	Int × 10^3 [K km/s]	V_{LSR} - $<V_{LSR}>^*$ [km/s]	$\sigma(v)^*$ [km/s]	T_{ex} * [K]	τ *	$N(H_2)$ × 10^{24} [cm^{-2}]	$M(H_2)$ [$M_\odot$]	$X(N_2H^+)^*$ × 10^{-10}
10	0.593	-1.26 ± 0.052	0.87 ± 0.038	11.03 ± 0.65	13.07 ± 0.74	4.62	4.01 ± 1.08	2.91
11	0.685	1.80 ± 0.032	1.29 ± 0.032	11.52 ± 2.11	3.14 ± 0.47	1.93	1.67 ± 0.45	0.34
12	0.669	0.70 ± 0.072	1.05 ± 0.061	10.64 ± 0.63	2.42 ± 0.39	1.83	1.59 ± 0.42	0.45
13	0.755	-2.05 ± 0.031	1.33 ± 0.030	13.67 ± 0.71	2.45 ± 0.20	2.01	1.74 ± 0.46	1.15
16	1.379	-0.67 ± 0.025	0.59 ± 0.020	10.96 ± 0.35	19.26 ± 1.07	5.37	4.67 ± 1.26	2.90
18	1.646	-1.79 ± 0.022	1.00 ± 0.016	17.06 ± 0.37	4.97 ± 0.24	4.98	4.33 ± 1.16	0.83
19	3.303	-2.43 ± 0.019	1.00 ± 0.017	21.21 ± 0.78	7.47 ± 0.27	8.99	7.82 ± 1.96	2.33
20	0.515	-2.19 ± 0.038	0.90 ± 0.026	10.16 ± 0.11	6.21 ± 0.44	4.04	3.51 ± 0.94	0.24
23	2.379	-1.56 ± 0.055	0.77 ± 0.034	22.40 ± 2.03	3.19 ± 0.27	5.52	4.80 ± 1.29	0.33

* Average measurements inside core regions.

as a good estimation based on the high uncertainties of the parameters used to estimate $N(N_2H^+)$, and of $X(N_2H^+)$. Additionally, we could consider the $M(H_2)$ mass estimation, derived from N_2H^+, more reliable due the better resolution. Which result is still consistent with the total mass measured in the protocluster zone in G351.77.

Additionally, we can provide new measurements inside the 1.3 mm core regions, such as column densities, H_2 masses, and N_2H^+ relative abundances, in addition to the parameters obtained from the line fitting process (see § 3), such as integrated intensities, excitation temperatures, optical depths, line widths, and centroid velocities (see Table 4.2.2), complementing the information of the Table E.11 in Louvet et al. submitted, and Table F.9 in Cunningham et al. (2023).

Chapter 5

Kinematics analysis

The main goal of our research is to analyze the kinematics of the dense gas within G351.77 protocluster, which is traced by N_2H^+. The spectral line fitting process detailed in § 3 provide us with the most reliable parameter we can measure over each spectra, the centroid velocity, with error estimations mostly lower than the 1%. This centroid velocity, coupled with the angular resolution of our data, enables us to analyze the kinematics of the protocluster at different scales. To achieve this, we utilize PV-diagrams, which allow us to characterize kinematic patterns providing information about the physical processes occurring at both small scales (core scales) and large scales (protocluster scale). These patterns may include inflow, rotation, outflow, or cloud-cloud collision features (Henshaw et al., 2014; Tobin et al., 2012; Mori et al., 2024; Haworth et al., 2015).

We utilize four parameters to generate the PV-diagrams. These parameters are the centroid velocity, integrated intensity, b and l coordinates (e.g. Hacar et al., 2018; Redaelli et al., 2019; Henshaw et al., 2014; González Lobos and Stutz, 2019; Álvarez-Gutiérrez et al., 2021). The first view of the PV-diagram of N_2H^+ emission in the G351.77 protocluster reveals distinct features along the filamentary structure (see Fig. 5.0.1), some of which appear to be consistent in position with the 1.3 mm band cores from the core catalog of Louvet et al. submitted, and consistent in the estimated velocity of these cores (see Table F.9 in Cunningham et al. (2023)). Moreover, we can distinguish two clear velocity structures in the PV-diagram, separated by $\sim$ 2 km/s. One of these velocity structures appears to be predominantly associated with the Bluest component, while the other seems to be

dominated by the Reddest component (see § 3.4 for further details). Furthermore, these two velocity structures seem to merge towards the northern region of the protocluster, going to the direction of the Mother filament extends.

The analysis at small scales provides clearer insights into the features observed in the PV-diagram. Specifically, we observe association with 1.3 mm band cores where we can distinguish two clear features:

1. The V-shape: where the core is positioned (or near) at the point where we measure the highest velocity of N_2H^+, and the surrounding gas transitions towards lower velocities (see Fig. 5.1.1, Fig. 5.1.2 and Fig. 5.1.3).

2. The Straight-shape: where the gas around the core transitions from high to low velocities, while the core is situated in the middle of this straight (see Fig. 5.1.4 and Figure 1 in Tobin et al. (2012)).

Several of these features are observed in the PV-diagram as part of the Bluest component and the Reddest component along the protocluster. Some of these features are even found without 1.3 mm cores detected. Additionally, we have measured the Velocity Gradients (VG) and timescales associated with these features in the regions with 1.3 mm band cores detected and without 1.3 mm band core detection (see below). These measurements, along with the $M(H_2)$ measured in § 4 provide us the opportunity to estimate mass inflow rates $\dot{M}(H_2)_{in}$ (see below). These measurements show us that the most prominent V-shape, that reaches speeds ~ 4.5 km/s, is consistent in position with a non-detected 1.3 mm band core, with an averaged $\dot{M}(H_2)_{in} \sim (4.08 \pm 0.81) \times 10^{-4}$ $M_\odot$/ yr.

On the other hand, analyzing the PV-diagrams at large scales reveals that the observed velocity structures shown in Fig. 5.0.1 are not only separated in velocity, but also by spatial position (see Fig. 5.2.1), where we can distinguish different N_2H^+ filamentary structures. In order to improve the analysis at large scale, we separate the protocluster into 4 different spatial regions (see Fig. 5.2.1):

- Two main filamentary structures where we locate most of the cores and observe the highest SNR values. The spectra within these filamentary structures are mostly fitted by 2-velocity-components. We refer to these filamentary structures as F1 and F2.

- A third filamentary structure situated to the south of F1, characterized by

mostly 2-velocity-components well defined with a Δv reaching $\sim$ 3 km/s. We designate this structure as F3.

- A small region to the north of the protocluster where F1 and F2 structures merge, identified as F4.

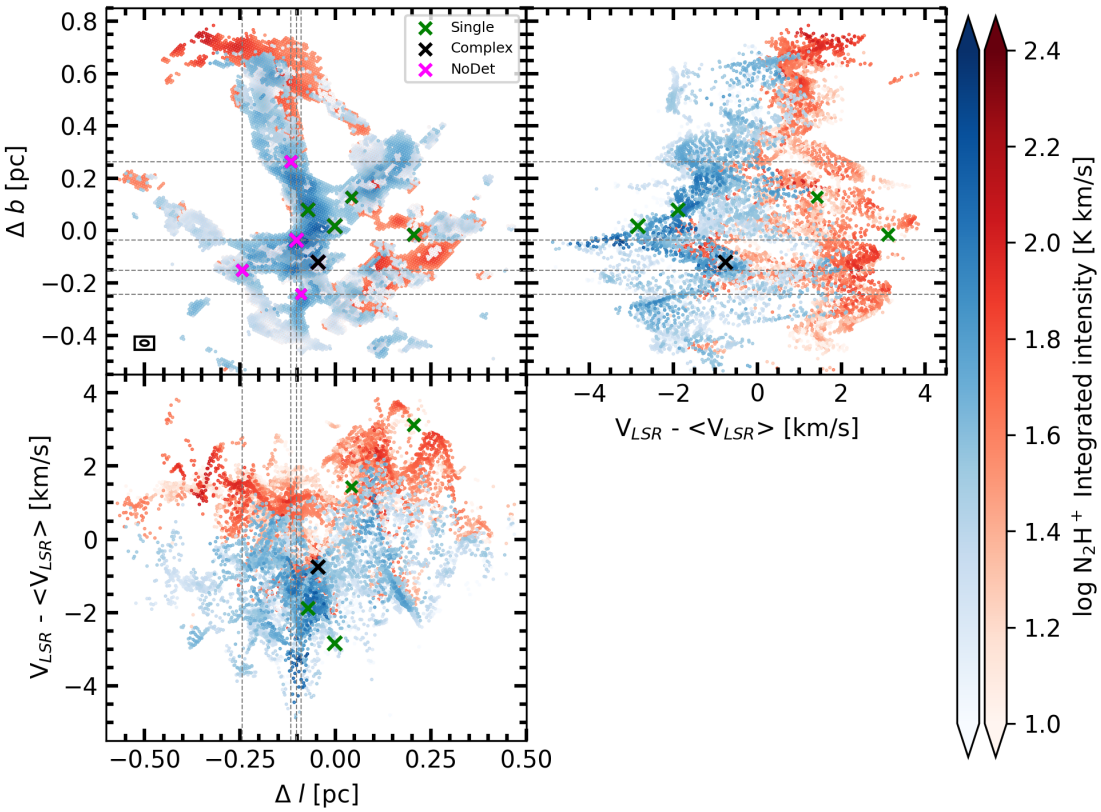

Figure 5.0.1: Top left: Spatial distribution of N_2H^+ of G351.77. The $\times$ markers indicate the position of the 1.3 mm band cores (Louvet et al. submitted). The green, black and magenta markers represent the spectral type of the cores; single, complex and non-detected, respectively (Cunningham et al., 2023). Dashed lines are used to extend the position of the non-detected cores to the other panels. The ellipse on bottom-left represent the beam size of N_2H^+ data. Top right and bottom: PV-diagrams. It is possible to observe multiple V-shapes or Straight-shapes along the filamentary structures, with some of them associated with cores in position and in velocity. The blue and red colorbar show the integrated intensity of N_2H^+ of the Bluest component and Reddest component, respectively. We can observe two clear and well-defined structures separated in velocities.

The separation of the protocluster into different spatial regions enables us to measure the VGs of each region in the PV-diagram, estimating the timescales and $\dot{M}(H_2)_{in}$ for each one (see Fig. 5.2.2). This approach delves deeper into the kinematics of the protocluster and establishes the relation between each region

and with the Mother filament.

5.1 Kinematics analysis at small scales

We analyze the N_2H^+ velocities around the 1.3 mm band cores within a radius 3 times the size of the core (see Table E.11 Louvet et al. submitted) to examine the behaviour of the surrounding gas while avoiding the overlap of gas around other cataloged cores. Subsequently, we re-create the PV-diagrams of N_2H^+ emission around these cores, aiming to identify features associated with them. From the 1.3 continuum data, 18 cores have been cataloged (see Table E.11, Louvet et al. submitted), with 9 of them located in zones with N_2H^+ emission (SNR > 9).

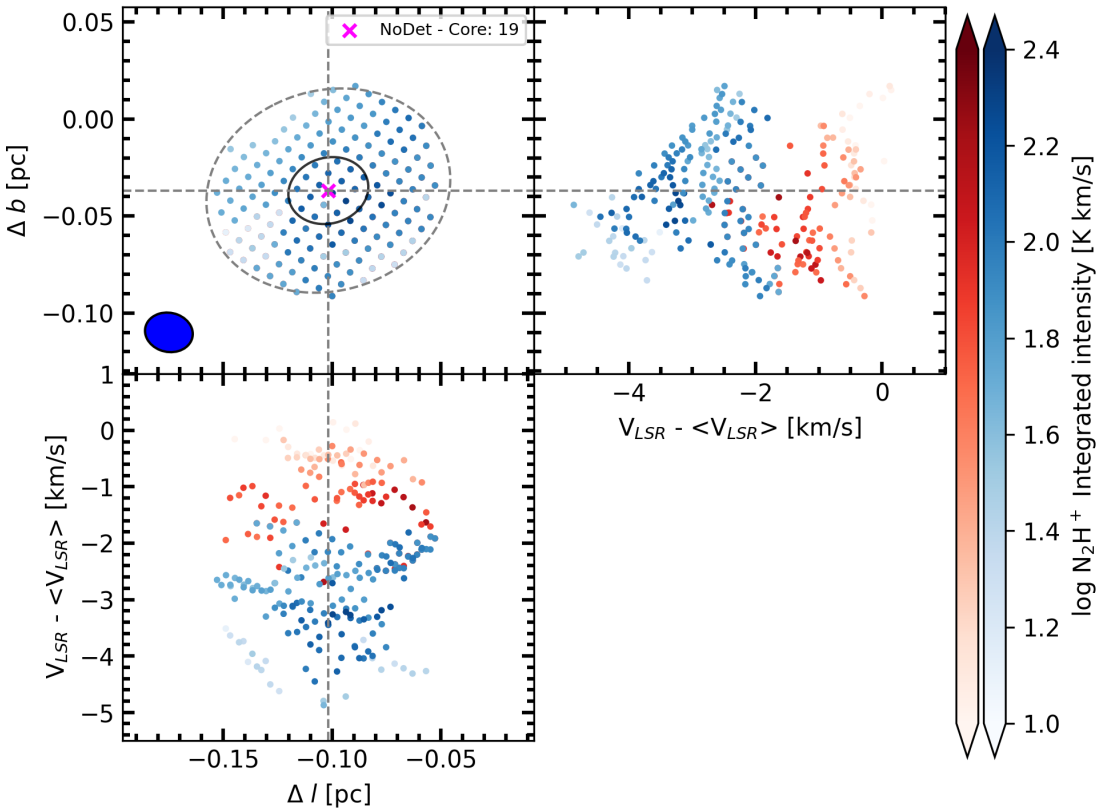

Figure 5.1.1: Top left: Position-Position diagram of a non-detected core from the core catalog of Louvet et al. submitted, and which we found the most prominent V-shape. The ellipse in the bottom-left corner represent the beam size of N_2H^+ data. Top right and bottom: PV-diagrams, where the blue and red colorbar represent the integrated intensity of the Bluest and the Reddest component, respectively. The dashed lines are used to extend the position of the non-detected core to the other panels.

However, only 6 cores have exhibited identifiable patterns (3 V-shapes and 3 Straight-shapes). To characterize the V-shapes, we applied a linear fit over the VGs involved at the borders of the distribution, encompassing the upper and bottom VG (see Fig. 5.1.2). These linear fits contemplate the position as a function of velocity, while the integrated intensity is utilized as a statistical weight. We propose that these points represent the inflowing gas with the highest velocity along a filamentary structure, where the filament assumes a leg-like shape with the core located at the knee (see Fig. 5.1.3).

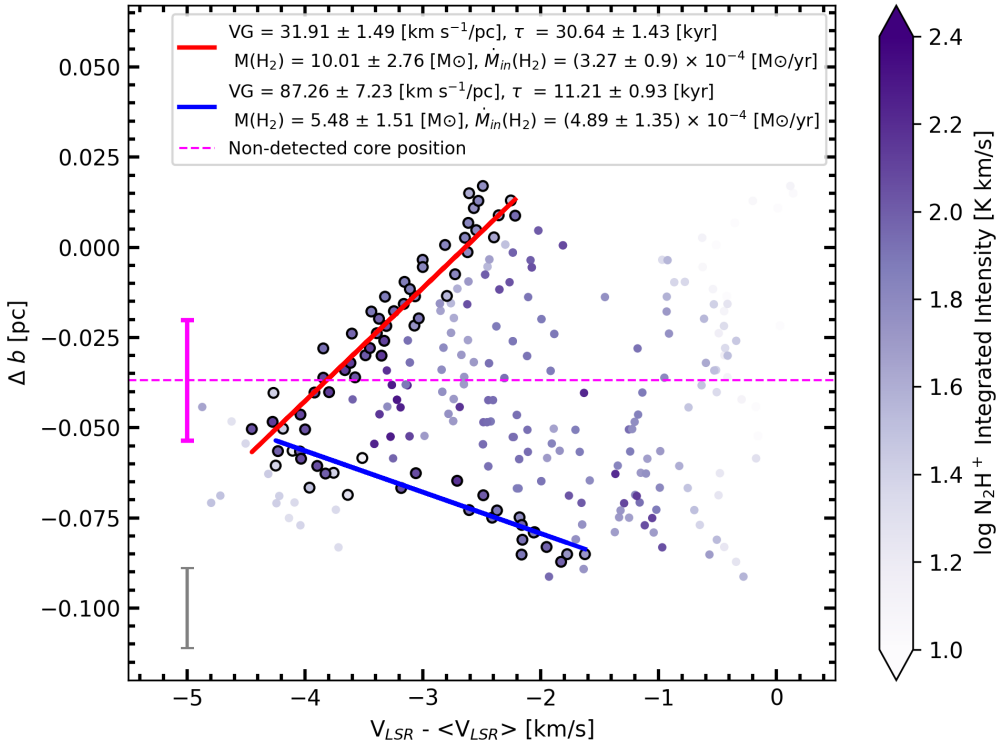

Figure 5.1.2: PV-diagram of the most prominent V-shape. The red and blue lines represent the line fit of the velocity gradients, which converge at $\sim$ 0.015 pc below of the central position of the core. The magenta errorbar represent the size of the core, while the horizontal dashed line, represent the position of the core. The colorbar is the integrated intensity of N_2H^+ without distinguishing between the Bluest or the Reddest component. The gray errorbar represent the beam size of the N_2H^+ data.

Once the VG have been measured, we can estimate the timescales associated with these VGs following the Eq. 5.1.1 (e.g. Álvarez-Gutiérrez et al., 2021). Furthermore, we can estimate the H_2 mass (§ 4) associated with the points used to measure the VGs in order to determinate the mass inflow rate $\dot{M}(H_2)_{in}$ following the Eq. 5.1.2.

$$\tau = \frac{1}{\mathrm{VG}} \tag{5.1.1}$$

$$\dot{\mathrm{M}}(\mathrm{H_2})_{in} = \frac{\mathrm{M}(\mathrm{H_2})}{\tau} \tag{5.1.2}$$

Focusing on the most prominent V-shape, we identify two clear VGs associated with a non-detected core (see Fig. 5.1.2). This core is located in the region with the highest N_2H^+ emission, where the spectra are fitted by 2-velocity-components. It is also located next to the central part of the protocluster, where we observe the continuum emission, along with the highest emission of molecules such as H_2CO, DCN, and HC_3N. This region also exhibits a concentration of cores without nearby N_2H^+ emission (see Cunningham et al., 2023; Ginsburg et al., 2022a, Louvet et al. submitted). We measure the VGs, timescales, mass, and mass inflow rate of the 6 features associated with the 1.3 mm band core, and we listed these parameters in Table 5.1.1.

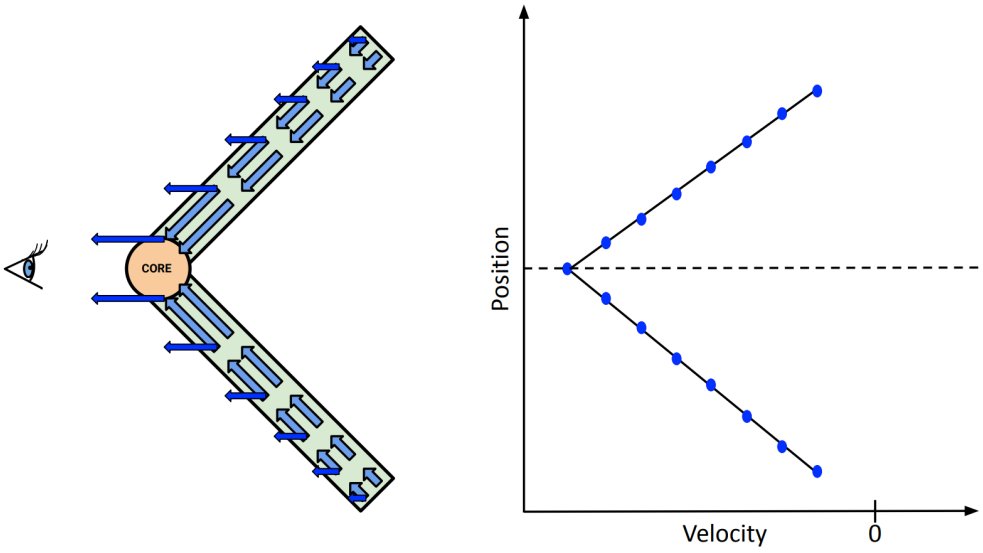

Figure 5.1.3: Left: Inflowing filamentary structure. The light blue and blue arrows represent the velocity magnitude of the gas and the radial component of the gas velocity, respectively. Right: PV-diagram of the inflowing filamentary structure. The blue points represent the highest velocity measured along the filament.

While the V-shapes associated with cores could be explained as inflowing gas within a filamentary structure, as depicted in Fig. 5.1.3, the Straight-shapes may be explained as a rotating filamentary structure (see Figure 1 in Tobin et al.

(2012)). This structure appears rotate following a solid-body rotation, with the core located in the middle of the filament and the velocity of the gas increasing towards the filament ends. However, filamentary structures with embedded cores have been observed in protoclusters, where the filaments inflow towards the inner and denser regions, and the cores follow the stream of the surrounding gas, inflowing with the filaments (Kim et al., 2022b; Arzoumanian et al., 2023; Lu et al., 2018; Motte et al., 2018).

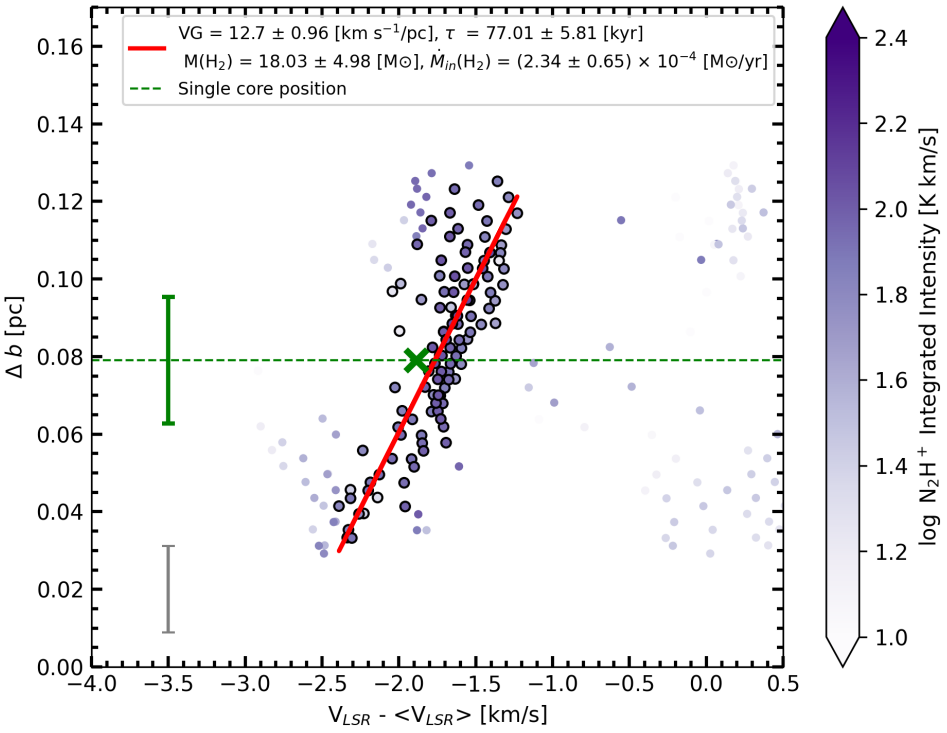

Figure 5.1.4: PV-diagram of a single core from the core catalog of Louvet et al. submitted. The feature describe what we define as a Straight-shape. The red line represent the line fit of the velocity gradient. The × marker indicate the position and the velocity of the core. The green errorbar shows the size of the core, while the gray errorbar represent the beam size.

Moreover, utilizing a Position-Position-Velocity diagram (PPV-diagram), we have cataloged 16 features found in the protocluster without associated 1.3 mm band cores. We have measured the VGs, timescales, mass, and $\dot{M}(H_2)_{in}$ (see Table 5.1.2) of these features. Given the integrated intensity measured in the regions where these features are observed and the estimated $\dot{M}(H_2)_{in}$, which appear similar to what we have estimated for the features associated with 1.3 mm band cores, we suggest a relation between these features and possible cores that are under the detection limit.

Table 5.1.1: Velocity gradients, timescales, H_2 mass, and mass inflow rate associated with the 1.3 mm band cores that present N_2H^+ features in the PV-diagram.

n	Shape	VG [km s^{-1}/pc]	Timescale [kyr]	M(H_2) [M_{dot}]	$\dot{M}(H_2)_{in}$ $\times 10^{-4}$ [$M_\odot$/yr]
13	Straight	26.89 ± 0.95	36.49 ± 1.29	9.66 ± 2.67	2.65 ± 0.73
16	V-shape	23.07 ± 2.76	42.39 ± 5.07	1.71 ± 0.47	0.40 ± 0.11
		22.67 ± 1.92	43.13 ± 3.65	5.44 ± 1.50	1.26 ± 0.35
18	Straight	12.70 ± 0.96	77.01 ± 5.81	18.03 ± 4.98	2.34 ±0.65
19	V-shape	31.91 ± 1.49	30.64 ± 1.43	10.01 ± 2.76	3.27 ± 0.90
		87.26 ± 7.23	11.21 ± 0.93	5.48 ± 1.51	4.89 ± 1.35
20	V-shape	23.99 ± 1.94	40.76 ± 3.30	1.02 ± 0.28	0.25 ± 0.07
		30.62 ± 3.63	31.93 ± 3.78	2.39 ± 0.66	0.75 ± 0.21
23	Straight	2.46 ± 0.14	397.63 ± 23.10	38.21 ± 10.56	0.96 ± 0.27

Table 5.1.2: Velocity gradients, timescales, H_2 mass, and mass inflow rate measured in N_2H^+ features found in the PV-diagram without the 1.3 mm band cores associated.

n	Shape	VG [km s^{-1}/pc]	Timescale [kyr]	M(H_2) [$M_\odot$]	$\dot{M}(H_2)_{in}$ $\times 10^{-4}$ [$M_\odot$/yr]
1	V-shape	33.04 ± 2.41	29.6 ± 2.16	15.29 ± 4.22	5.17 ± 1.43
		48.05 ± 6.21	20.35 ± 2.63	12.44 ± 3.44	6.11 ± 1.69
2	V-shape	33.34 ± 2.19	29.32 ± 1.93	17.97 ± 4.96	6.13 ± 1.69
		44.40 ± 3.53	22.02 ± 1.75	17.11 ± 4.72	7.77 ± 2.14
3	V-shape	58.51 ± 10.24	16.71 ± 2.92	6.58 ± 1.82	3.94 ± 1.09
		22.52 ± 1.03	43.42 ± 1.99	23.65 ± 6.53	5.45 ± 1.50
4	V-shape	19.11 ± 1.65	51.17 ± 4.41	13.21 ± 3.64	2.58 ± 0.71
		22.49 ± 2.32	43.47 ± 4.49	12.45 ± 3.44	2.86 ± 0.79
5	V-shape	24.35 ± 2.73	40.16 ± 4.50	4.81 ± 1.32	1.20 ± 0.33
		37.54 ± 4.13	26.05 ± 2.86	7.59 ± 2.09	2.91 ± 0.80
6	Straight	24.35 ± 2.73	40.16 ± 4.50	18.58 ± 5.13	4.63 ± 1.28
7	V-shape	16.10 ± 1.38	60.75 ± 5.19	7.16 ± 1.97	1.18 ± 0.32
		15.30 ± 2.81	63.92 ± 11.73	2.41 ± 0.66	0.38 ± 0.10
8	V-shape	17.77 ± 1.19	55.01 ± 3.68	22.79 ± 6.29	4.14 ± 1.14
		11.18 ± 0.78	87.43 ± 6.13	23.45 ± 6.48	2.68 ± 0.74
9	V-shape	11.06 ± 0.90	88.40 ± 7.16	13.51 ± 3.73	1.53 ± 0.42
		17.23 ± 3.55	56.76 ± 11.70	6.14 ± 1.69	1.08 ± 0.30
10	Straight	25.32 ± 1.13	38.62 ± 1.72	45.64 ± 5.08	11.82 ± 1.32
11	V-shape	17.75 ± 1.61	55.08 ± 4.99	5.08 ± 1.41	0.92 ± 0.26
		20.91 ± 1.88	46.77 ± 4.20	2.33 ± 0.64	0.50 ± 0.14
12	V-shape	20.47 ± 1.23	47.77 ± 2.86	12.76 ± 3.52	2.67 ± 0.74
		33.46 ± 2.60	29.23 ± 2.27	10.65 ± 2.94	3.64 ± 1.01
13	V-shape	20.49 ± 2.41	47.72 ± 5.60	10.53 ± 2.91	2.21 ± 0.61
		35.59 ± 4.61	29.23 ± 3.56	9.17 ± 2.53	3.14 ± 0.87
14	V-shape	12.55 ± 1.04	77.90 ± 6.43	3.18 ± 0.88	0.41 ± 0.11
		34.67 ± 2.44	28.20 ± 1.98	3.62 ± 1.01	1.28 ± 0.36
15	V-shape	48.40 ± 3.80	20.20 ± 1.58	8.81 ± 2.43	4.36 ± 1.20
		42.72 ± 4.74	22.89 ± 2.54	5.01 ± 1.38	2.19 ± 0.60
16	V-shape	12.27 ± 1.35	79.70 ± 8.74	9.08 ± 2.51	1.14 ± 0.31
		16.56 ± 2.11	59.03 ± 7.53	8.22 ± 2.27	1.39 ± 0.38

5.2 Kinematics analysis at large scales

Examining the PV-diagram of the N_2H^+ emission at large scale reveals two distinct large scale structures, each separated by velocity in $\sim$ 2 km/s. The averaged centroid velocities for these structures are $\sim$ -1 km/s and 1 km/s, respectively. One of them appears to be dominated by the Bluest component, while the other is characterized by the Reddest component. These large-scale structures present features like a zig-zag along the protocluster, which we suggest produced by kinematic effects at smaller scales (see § 5.1). However, upon deeper examination of the kinematic and inspection of the PPV-diagram, we realize that these large-scale structures are separated both by velocity and spatially simultaneously. In order to distinguish each structure, we have divided the N_2H^+ emission of G351.77 protocluster into 4 regions based on its spatial location (see Fig. 5.2.1).

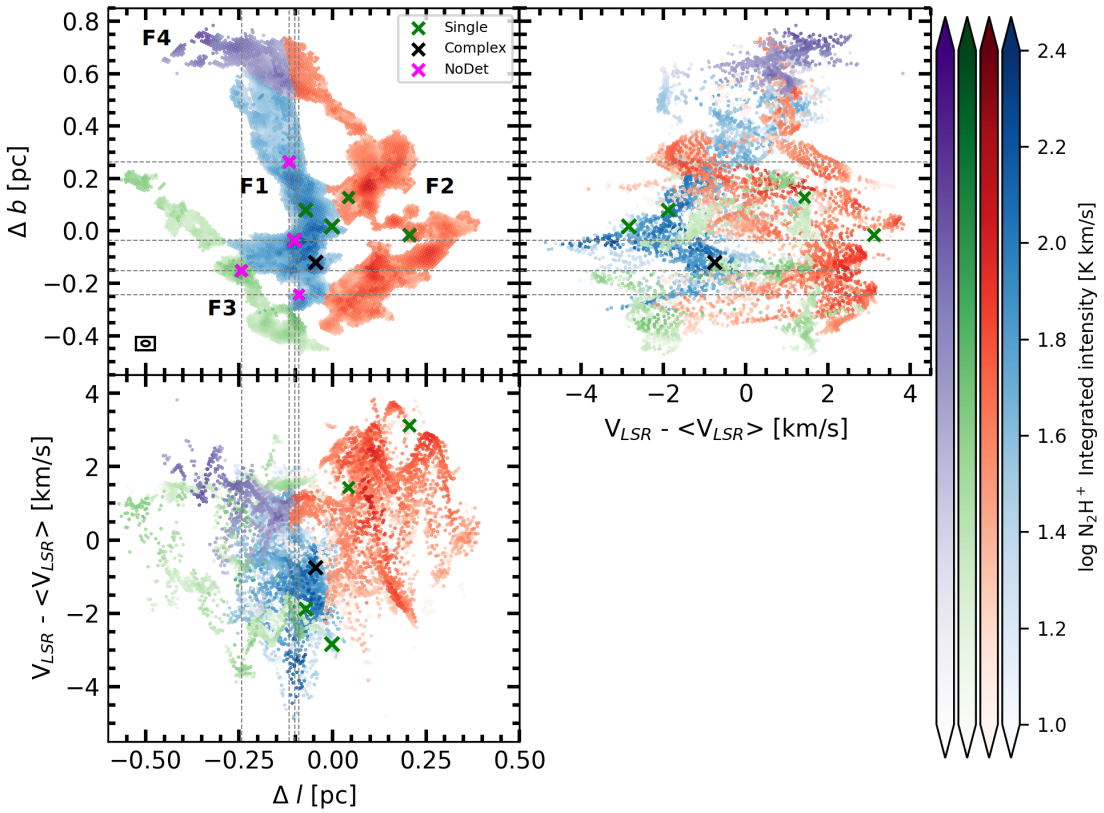

Figure 5.2.1: Same caption of Fig. 5.0.1. The blue, red, green and purple colorbar represent the N_2H^+ integrated intensity of the F1, F2, F3, and F4 structure.

- F1 structure: This corresponds to the primary filamentary structure within the protocluster, where we observe the highest values of SNR, integrated

intensity and column densities. It is connected with the 3 other large-scale structures defined within the protocluster. Furthermore, 6 out of the 9 cores located in regions with N_2H^+ emission are situated within this filamentary structure. Notably, the most prominent V-shape and the 3 Straight-shapes are located within this structure. Most of spectra in this structure are fitted by 2-velocity-components.

- F2 structure: Adjacent to the F1 structure, the F2 structure the second primary filamentary structure within the protocluster. It connects to the F1 structure near to the protocluster's center through regions with low SNR and integrated intensity, but it merges with the F1 structure towards the north of the protocluster. This structure appears as a twisted filament, less defined as the F1. Nonetheless, two 1.3 mm band cores situated in regions with N_2H^+ emission, and several V- and Straight-shapes are positioned within this structure. Multiple spectra within this structure are fitted by 2-velocity-components.

- F3 structure: Positioned to the south of the F1 structure, this filamentary structure displays 2 clear velocity components along its length. It contains one 1.3 mm band core, coinciding with the position where the filament exhibits a large-scale V-shape in the PV-diagram.

- F4 structure: Situated in the northern region of the protocluster, where the F1 and F2 structures merge, the F4 structure present well defined V- and Straight-shapes. This regions is connected with the Mother filament.

The PV-diagram at large scale, separated by spatial structures, reveals clear large-scale features, which we can observe clear VGs. Employing a similar method as in § 5.1 we measure VGs applying a linear fit to the distribution (see Fig. 5.2.2). This approach enables the estimation of timescale and $\dot{M}(H_2)_{in}$ associated with these large-scale structures (see Table 5.2.1). We have identified 10 large-scale VGs within the protocluster (see Fig. 5.2.2), which we have designated as follows:

- B1 and B2 for the VGs associated with the F1 structure.

- R1, R2, and R3 for the VGs associated with the F2 structure.

- G1, G2, and G3 for the VGs associated with the F3 structure.

- P1 and P2 for the VGs associated with the F4 structure.

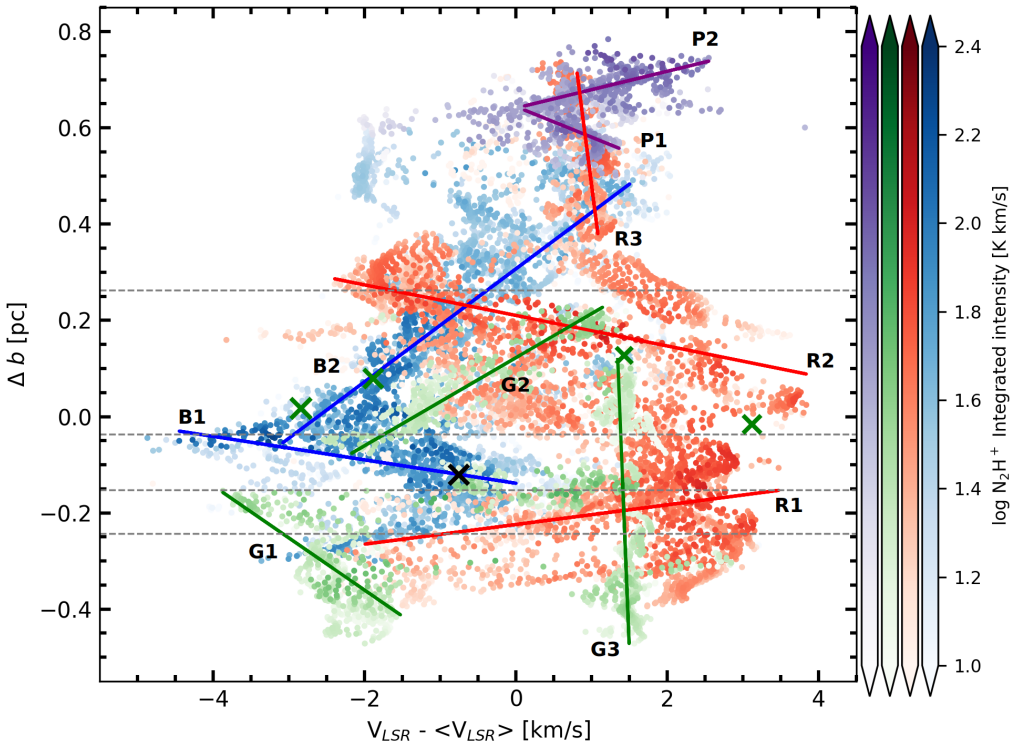

Figure 5.2.2: PV-diagram of N_2H^+ emission separated by spatial distribution. The blue, red, green, and purple colorbar represent the F1, F2, F3, and F4 spatial structure, respectively, shown in Fig. 5.2.1. The blue, red, green and purple solid lines represent the VGs measured in the F1, F2, F3 and F4 large scale structures, respectively. The dashed horizontal lines represent the position of non-detected cores, while the green and black × markers represent the single and complex cores, respectively.

From these VGs and their spatial position, we can infer kinematic processes influencing these large-scale structures, as follows:

1. VGs B1 and B2 exhibit two large-scale velocity distribution converging near the position of a non-detected core, where we observe the most prominent V-shape (see § 5.1). Furthermore, along these velocity distribution, we find four 1.3 mm band cores and several small-scales features that we suggest represent cores under the detection limit (see § 5.1).

2. VGs R1 and R2 display two large-scale velocity distribution, but less well defined than those observed in B1 and B2. Although these VGs do not converge at a specific position or velocity, they apparently reach opposite velocities to the most prominent V-shape (see Fig. 5.1.2). VG R3 looks constant in velocity but presents several of small-scale features such as

V-shapes.

3. VGs G1 and G2 show two large-scale velocity distributions that, although they do not converge, appear to point towards the direction of a non-detected core. VG G3 looks constant in velocity but presents a few small-scale features like V-shapes.

4. VGs P1 and P2 display two large-scale velocity distribution. P1 exhibits the velocity distribution connected to the F1 and F2 structure, while P2 shows the velocity distribution connected to the Mother filament.

Table 5.2.1: Velocity gradients, timescales, H_2 mass, and mass inflow rate measured for each large scale N_2H^+ feature in the PV-diagram.

n	VG [km s^{-1}/pc]	Timescale [kyr]	M(H_2) [$M_\odot$]	$\dot{M}(H_2)_{in}$ $\times 10^{-3}$ [$M_\odot$/yr]
B1	41.06 ± 1.95	23.8 ± 1.13	81.0 ± 22.4	3.40 ± 0.95
B2	8.52 ± 0.08	114.7 ± 1.17	153.3 ± 42.4	1.33 ± 0.37
R1	48.94 ± 5.63	20.0 ± 2.30	187.9 ± 51.9	9.39 ± 2.81
R2	31.51 ± 1.19	31.0 ± 1.17	141.1 ± 39.0	4.55 ± 1.27
R3	1.21 ± 0.15	803.4 ± 104.0	69.7 ± 19.3	0.08 ± 0.02
G1	9.22 ± 0.34	105.9 ± 3.95	22.0 ± 6.0	0.20 ± 0.05
G2	3.93 ± 0.60	248.4 ± 38.4	28.9 ± 8.0	0.11 ± 0.03
G3	0.09 ± 0.00	10689.1 ± 220.2	83.8 ± 23.1	0.007 ± 0.002
P1	15.70 ± 1.15	62.2 ± 4.55	30.7 ± 8.5	0.49 ± 0.14
P2	26.17 ± 1.14	37.3 ± 1.63	75.6 ± 20.9	2.02 ± 0.56

The highest VGs and $\dot{M}(H_2)_{in}$ are observed in the 2 main filamentary structures (F2 and F1, respectively), whereas the lowest VGs and $\dot{M}(H_2)_{in}$ are measured in the F3 filamentary structure. These differences may indicate that certain region within the protocluster are experimenting higher levels of star formation activity, which is consistent with the position of the 1.3 mm band cores and the cataloged small-scales features.

Chapter 6

Discussion

In the § 5.1 we characterized the features associated with the 1.3 mm band cores and features without 1.3 mm band cores, suggesting that N_2H^+ is inflowing to cores or with cores embedded (Kim et al., 2022b; Arzoumanian et al., 2023; Lu et al., 2018; Motte et al., 2018). Additionally, in § 5.2 we divided the N_2H^+ emission of the G351.77 protocluster by spatial regions. These structures have been characterized by measuring VGs, timescales, and $\dot{M}(H_2)_{in}$.

From the analysis of the kinematic at large scale (see § 5.2) we realize that the F1 filamentary structure is inflowing towards the non-detected core, where we observe the most prominent V-shape in the PV-diagram, suggesting that this gas comes from outside the protocluster. Furthermore, we find 1.3 mm band cores associated with Straight-shapes in G351.77 protocluster are located in the middle of the F1 filament structure, near to the position where we observe the most prominent V-shape. Considering the velocity distribution of N_2H^+ displayed in the PV-diagrams of Straight-shapes, their location, and the consistency of the N_2H^+ velocities with the velocity measured for the cores (see Table F.9 in Cunningham et al. 2023), we propose that these cores are inflowing towards the location of the most prominent V-shape, entrained in the potential slow contraction of the protocluster (Kim et al., 2022b; Arzoumanian et al., 2023; Lu et al., 2018; Motte et al., 2018). All this, in addition with the measured $\dot{M}(H_2)_{in}$, suggest that the F1 structure is actively forming stars.

In contrast to the F1, the F2 filamentary structure does not show evidence of inflowing gas towards a specific location but rather presents inflow towards different

locations along the structure. Moreover, most of the features (which we suggest associated with cores under the detection limit) are located within it. In addition, with the highest $\dot{M}(H_2)_{in}$, this could suggest that the F2 structure presents equal or more star formation activity than F1 structure.

The F3 filamentary structure shows few evidence of star formation activity within it, where we find 1 non-detected core and 3 features without 1.3 mm band core associated. However, the measured VGs suggest that the non-detected core is strongly affecting the filamentary structure, which features indicate that the gas in this filament is inflowing towards the non-detected core location.

The F4 structure present one of the highest $\dot{M}(H_2)_{in}$ estimations, which along with the velocity distribution, could suggest that the gas that is inflowing to the protocluster from outside, may also be forming star.

In order to complement and enhance understanding of the kinematic processes occurring in the protocluster at large scales, we complement the PV-diagram analysis making use of H_2CO and DCN tracers (see § Appendix C), which coverage the central part of the protocluster without N_2H^+ emission (Motte et al., 2022; Cunningham et al., 2023). Additionally, we modeled rotating, infalling, and rotating and infalling spheres (see § Appendix C), whose radial velocities are use to recreate PV-diagrams (Henshaw et al., 2014; Tobin et al., 2012; Mori et al., 2024). This allowed us to analyze the features and velocities present in these diagrams and how they describe the kinematic.

Fig. 6.0.1 shows the PV-diagram of N_2H^+ and H_2CO in comparison with the contours of a rotating and infalling sphere. We observe that H_2CO reaches $\Delta v \sim 13$ km/s, with its velocity peaks in the PV-diagram aligning well with the contours of the model. Furthermore, upon examining the velocity distribution of DCN in the PV-diagram, we observe similar features with H_2CO (see Fig. C.0.5 and Fig. C.0.6), which appear to correspond with the model of the rotating and infalling sphere. Based on the spatial locations of H_2CO and DCN, along with the features in the PV-diagrams described by our model, we suggest large-scale rotation and infall process in the center of the protocluster (Tobin et al., 2012; Mori et al., 2024).

This scenario suggest that the 2 clear velocity structures observed in Fig. 5.0.1 are rotating parallel to the direction of the Mother filament, although the inflow

process seems more dominant. On the other hand, analyzing the model of rotation and infall by separate, the rotating sphere models in a better way the large scale shapes presents in H_2CO and DCN, suggesting that the central part of the protocluster is more dominated by rotation than infall (see Fig. C.0.11, Fig. C.0.12, Fig. C.0.8, and Fig. C.0.9).

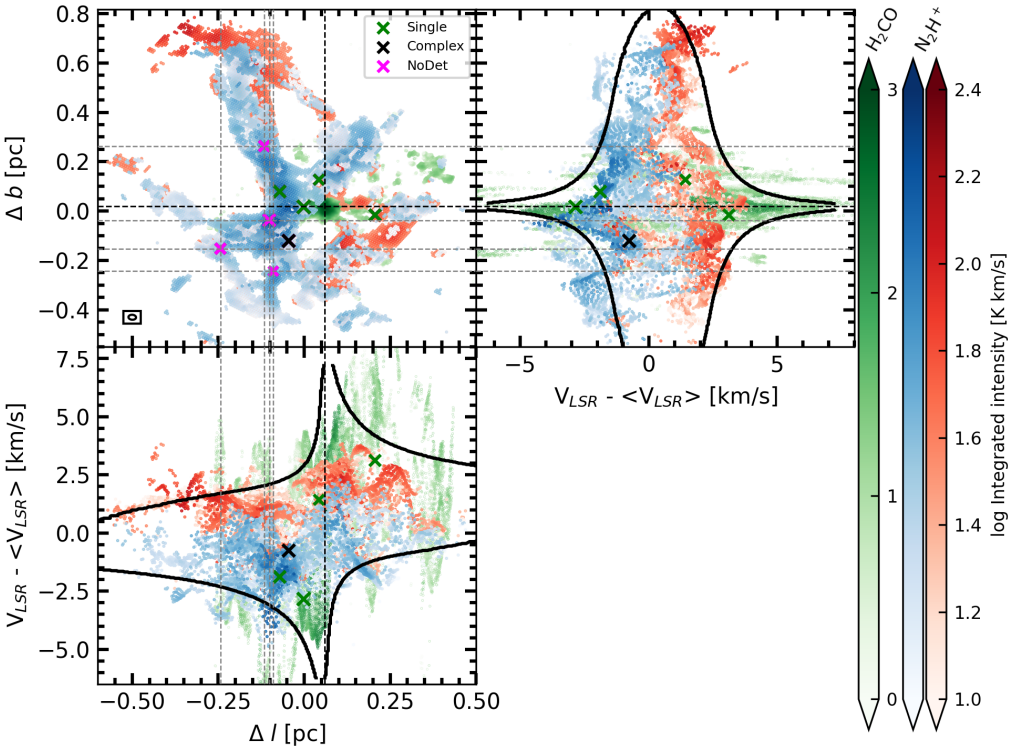

Figure 6.0.1: PV-diagram of N_2H^+ emission separated by spatial distribution. The blue, red, green, and purple colorbar represent the F1, F2, F3, and F4 spatial structure, respectively, shown in Fig. 5.2.1. The blue, red, green and purple solid lines represent the VGs measured in the F1, F2, F3 and F4 large scale structures, respectively. The dashed horizontal lines represent the position of non-detected cores, while the green and black × markers represent the single and complex cores, respectively

Nevertheless, the sphere used to obtain the models employs a mass of 270 $M_\odot$, which is 10 times lower than the mass measured inside of radius of 0.8 pc in G351.77, which is $\sim$ 2720 $M_\odot$. This difference of mass affect directly to the radial velocities measured in our models, going from $\Delta v \sim 14$ km/s to $\Delta v \sim 44$ km/s. That is, underestimated velocities by a factor of ~ 3. However, although the radial velocities present differences, the shapes observed in the PV-diagram are still the same, which suggest that these shapes just depend of the kinematic process (Kim et al., 2022b; Arzoumanian et al., 2023; Lu et al., 2018).

The velocities measured for N_2H^+, H_2CO and DCN seems to be similar, and the features observed in the PV-diagram of H_2CO and DCN seems describe the same kinematic process. All of this indicates that the measurements are reliable. However, the modeled sphere suggests higher velocities than the observed, raising questions such as: Why we measure lower velocities in the protocluster? What other physical processes are affecting the kinematics of the gas? Current evidence provides that processes such as infall and rotation are occurring at smaller scales that in cores oh the central part of the protocluster (Zapata et al., 2008; Leurini et al., 2014, 2013, 2011b, 2008a,b; Klaassen et al., 2015; Antyufeyev et al., 2016). Additionally, bipolar outflows associated with YSOs in the center of G351.77 have been cataloged. Moreover, the fragmentation into clumps observed along the Mother filament have been attributed as triggered by turbulences and magnetic fields produced by the high-mass star formation (Sabatini et al., 2019; Yu et al., 2018; Leurini et al., 2019, 2011a). Considering all these physical processes, we could suggest that the kinematic behaviour of the gas traced by N_2H^+, H_2CO and DCN may not be as described in our model, which only considers 2 kinematic processes.

Chapter 7

Conclusions

We conducted an analysis of the kinematics of the dense and cold gas within the massive G351.77 protocluster, traced by the spectral line N_2H^+, utilizing the PV-diagrams and characterization of physical processes involved in high-mass star formation. The spatial resolution of the N_2H^+ data cube is $\sim$ 4000 AU, making this the first study of this kind in G351.77.

Initially, we utilized specialized software, PySpecKit, to fit the N_2H^+ spectra, which provided key physical parameters such as excitation temperature, optical depth, centroid velocity, and line width. These parameters were subsequently utilized in our analysis. Additionally, we performed an experiment to determinate the SNR that require the spectra to obtain reliable models. We have implemented the spectral line fitting over the entire data, fitting 1- and 2-velocity components. Later, we developed a method two define and maintain each spectra with 1- or 2-velocity component, based on the line width and SNR of the modeled spectra. Finally obtaining a modeled data that posses spectra with 1- or 2-velocity components. Based on the centroid velocity distribution of each spectra, we divided the data into 2 velocity components, which we named the Bluest component and Reddest component.

The excitation temperature, optical depth, and line width obtained from the spectral line fitting enable the estimation of column density maps and masses of N_2H^+. Additionally, we utilize the column density map of H_2 provided by Dell'Ova et al submitted, to estimate the relative abundance of N_2H^+ ($X(N_2H^+)$). However, due the difference of angular resolution between the column density map

of N_2H^+ and H_2, we convolved the N_2H^+ data, reducing its angular resolution to the same as the column density map of H_2. Subsequently, we estimated an N_2H^+ relative abundance $\sim (1.66 \pm 0.46) \times 10^{-10}$, from which we derived an estimated H_2 mass in the protocluster $\sim 1660 \pm 458$ $M_\odot$.

The centroid velocity measured by PySpecKit allows the characterization of kinematic patterns at different scales. To achieve this, we implemented the analysis of the PV-diagram, identifying different small and large scales features. Among the most significant results obtained from the PV-diagrams are:

1. The PV-diagram at small scales reveals features such as V- and Straight-shapes associated in position and in velocity with the 1.3 mm band cores cataloged. These features have been characterized measuring the VGs, timescales, mass and $\dot{M}(H_2)_{in}$. The most prominent V-shape reaches velocities $\sim$ -4.5 km/s, whose averaged $\dot{M}(H_2)_{in} \sim 4.08 \times 10^{-4}$ $M_\odot$/yr and an averaged timescale $\sim$ 20.92 kyr.

2. Similarly, the PV-diagram at small scales reveals features such as V- and Straight-shapes without 1.3 mm band cores associated. We have characterized these features measuring the VGs, timescales, mass and $\dot{M}(H_2)_{in}$. Based on the position-position of these features and their characterizations, we suggest that they are formed by cores that are under the detection limit.

3. We propose that the V-shapes describe inflowing gas in filamentary structures where the cores is located near to vertex of the V-shapes. While that the Straight-shapes describe inflowing filamentary structures with cores following the stream produced by the gas.

4. The PV-diagram at large scales reveals 2 velocity structures, which reach averaged velocities $\sim$ -1 and 1 km/s, respectively. The separation of the N_2H^+ emission by spatial location reveals that these 2 velocity structures are in different locations in the protocluster.

5. Large scale features are found within each spatial structure in the protocluster, which have been characterized measuring VGs, timescales, mass and $\dot{M}(H_2)_{in}$. Based on this characterization, we suggest what spatial structures reveal more star formation activity.

6. The analysis of large scale VGs reveals that one filamentary structure is inflowing towards a core position, where we observe the most prominent V-shape in the PV-diagram at small scale. This filamentary structure present several of cores and features that we suggest as cores, suggesting that they are inflowing along with the filament.

We have complemented the PV-diagram analysis with the H_2CO and DCN tracers, which cover areas without N_2H^+ emission. This allows to explore the relations between the large-scale kinematics described by N_2H^+ and the central region of the protocluster. In addition, we have implemented a rotating and infalling sphere model in order to characterize the PV-diagram features produced by these kinematic processes, which is consistent with previous work (e.g. Henshaw et al., 2014; Tobin et al., 2012; Mori et al., 2024).

The PV-diagram features produced by H_2CO and DCN suggest that the central region of the protocluster may be experiencing simultaneous rotating and infalling, where the rotation appears to be the most dominant kinematic effect. On the other hand, considering the velocity distribution and the position-position of the 2 large-scale velocity structures of N_2H^+ separated by ~ 2 km/s in the PV-diagram, in addition with the possible rotation features described by H_2CO and DCN, we suggest that these 2 large-scale velocity structures could be rotating relative to each other, with the rotating axis parallel to the direction of the maternal filament. However, the most prominent kinematic process present at the N_2H^+ filamentary structures corresponds appears to be inflow, which seems to be inflowing not towards the center of the protocluster, but rather inflowing onto themselves towards denser N_2H^+ regions.

Nevertheless, while the shapes and features presented in the model are consistent with those observed in the PV-diagram by the tracers, the measured velocities exhibit inconsistent with the velocities of returned by the models in a factor of 3. We attribute these differences to the simplicity of the model, which only considers 2 kinematic effects. Whereas, different researches suggest the presence of rotation and infall at small scales, bipolar outflows produced by YSOs, gravitational instabilities along the filament, and magnetic fields produced by the high-mass star formation in the protocluster, whose physical effect could be strongly affecting the behaviour of the gas.

Bibliography

Álvarez-Gutiérrez, R. H., Stutz, A. M., Law, C. Y., Reissl, S., Klessen, R. S., Leigh, N. W. C., Liu, H. L., and Reeves, R. A. (2021). Filament Rotation in the California L1482 Cloud. , 908(1):86.

André, P., Arzoumanian, D., Könyves, V., Shimajiri, Y., and Palmeirim, P. (2019). The role of molecular filaments in the origin of the prestellar core mass function and stellar initial mass function. , 629:L4.

Anirudh, R., Eswaraiah, C., Jiao, S., and Jose, J. (2023). Role of magnetic fields in the fragmentation of the Taurus B213 filament into Sun-type star-forming cores. *Journal of Astrophysics and Astronomy*, 44(2):59.

Antyufeyev, O. V., Shulga, V. M., and Zinchenko, I. I. (2016). Bipolar molecular outflow in IRAS 17233-3606. *Kinematics and Physics of Celestial Bodies*, 32(6):276–282.

Arzoumanian, D., Arakawa, S., Kobayashi, M. I. N., Iwasaki, K., Fukuda, K., Mori, S., Hirai, Y., Kunitomo, M., Kumar, M. S. N., and Kokubo, E. (2023). Insights on the Sun Birth Environment in the Context of Star Cluster Formation in Hub-Filament Systems. , 947(2):L29.

Bally, J., Langer, W. D., Stark, A. A., and Wilson, R. W. (1987). Filamentary Structure in the Orion Molecular Cloud. , 312:L45.

Bergin, E. A., Ciardi, D. R., Lada, C. J., Alves, J., and Lada, E. A. (2001). Molecular Excitation and Differential Gas-Phase Depletions in the IC 5146 Dark Cloud. , 557(1):209–225.

Beuther, H., Walsh, A. J., Johnston, K. G., Henning, T., Kuiper, R., Longmore, S. N., and Walmsley, C. M. (2017). Fragmentation and disk formation in high-mass star formation: The ALMA view of G351.77-0.54 at 0.06" resolution. , 603:A10.

Bonne, L., Bontemps, S., Schneider, N., Clarke, S. D., Arzoumanian, D., Fukui, Y., Tachihara, K., Csengeri, T., Guesten, R., Ohama, A., Okamoto, R., Simon, R., Yahia, H., and Yamamoto, H. (2020). Formation of the Musca filament: evidence for asymmetries in the accretion flow due to a cloud-cloud collision. , 644:A27.

Brouillet, N., Despois, D., Molet, J., Nony, T., Motte, F., Gusdorf, A., Louvet, F., Bontemps, S., Herpin, F., Bonfand, M., Csengeri, T., Ginsburg, A., Cunningham, N., Galván-Madrid, R., Maud, L., Busquet, G., Bronfman, L., Fernández-López, M., Jeff, D. L., Lefloch, B., Pouteau, Y., Sanhueza, P., Stutz, A. M., and Valeille-Manet, M. (2022). ALMA-IMF. IV. A comparative study of the main hot cores in W43-MM1: Detection, temperature, and molecular composition. , 665:A140.

Busquet, G., Estalella, R., Zhang, Q., Viti, S., Palau, A., Ho, P. T. P., and Sánchez-Monge, Á. (2011). N_2H^+ depletion in the massive protostellar cluster AFGL 5142. , 525:A141.

Caselli, P., Myers, P. C., and Thaddeus, P. (1995). Radio-astronomical Spectroscopy of the Hyperfine Structure of N 2H +. , 455:L77.

Caselli, P., Walmsley, C. M., Zucconi, A., Tafalla, M., Dore, L., and Myers, P. C. (2002a). Molecular Ions in L1544. I. Kinematics. , 565(1):331–343.

Caselli, P., Walmsley, C. M., Zucconi, A., Tafalla, M., Dore, L., and Myers, P. C. (2002b). Molecular Ions in L1544. II. The Ionization Degree. , 565(1):344–358.

Cunningham, N., Ginsburg, A., Galván-Madrid, R., Motte, F., Csengeri, T., Stutz, A. M., Fernández-López, M., Álvarez-Gutiérrez, R. H., Armante, M., Baug, T., Bonfand, M., Bontemps, S., Braine, J., Brouillet, N., Busquet, G., Díaz-González, D. J., Di Francesco, J., Gusdorf, A., Herpin, F., Liu, H., López-Sepulcre, A., Louvet, F., Lu, X., Maud, L., Nony, T., Olguin, F. A., Pouteau, Y., Rivera-Soto, R., Sandoval-Garrido, N. A., Sanhueza, P., Tatematsu, K., Towner, A. P. M., and Valeille-Manet, M. (2023). ALMA-IMF VII – First release of the full spectral line cubes:Core kinematics traced by DCN J=(3-2). *arXiv e-prints*, page arXiv:2306.14710.

Daniel, F., Dubernet, M. L., Meuwly, M., Cernicharo, J., and Pagani, L. (2005). Collisional excitation rate coefficients of N_2H^+ by He. , 363(4):1083–1091.

Fontani, F., Caselli, P., Crapsi, A., Cesaroni, R., Molinari, S., Testi, L., and Brand, J. (2006). Searching for massive pre-stellar cores through observations of $N2H^+$ and $N2D^+$. , 460(3):709–720.

Ginsburg, A., Csengeri, T., Galván-Madrid, R., Cunningham, N., Álvarez-Gutiérrez, R. H., Baug, T., Bonfand, M., Bontemps, S., Busquet, G., Díaz-González, D. J., Fernández-López, M., Guzmán, A., Herpin, F., Liu, H., López-Sepulcre, A., Louvet, F., Maud, L., Motte, F., Nakamura, F., Nony, T., Olguin, F. A., Pouteau, Y., Sanhueza, P., Stutz, A. M., Towner, A. P. M., ALMA-IMF Consortium, Armante, M., Battersby, C., Bronfman, L., Braine, J., Brouillet, N., Chapillon, E., Di Francesco, J., Gusdorf, A., Izumi, N., Joncour, I., Walker Lu, X., Men'shchikov, A., Menten, K. M., Moraux, E., Molet, J., Mundy, L., Nguyen Luong, Q., Reyes-Reyes, S. D., Robitaille, J., Rosolowsky, E., Sandoval-Garrido, N. A., Svoboda, B., Tatematsu, K., Walker, D. L., Whitworth, A.,

Wu, B., and Wyrowski, F. (2022a). ALMA-IMF. II. Investigating the origin of stellar masses: Continuum images and data processing. , 662:A9.

Ginsburg, A. and Mirocha, J. (2011). PySpecKit: Python Spectroscopic Toolkit. Astrophysics Source Code Library, record ascl:1109.001.

Ginsburg, A., Sokolov, V., de Val-Borro, M., Rosolowsky, E., Pineda, J. E., Sipőcz, B. M., and Henshaw, J. D. (2022b). Pyspeckit: A Spectroscopic Analysis and Plotting Package. , 163(6):291.

González Lobos, V. and Stutz, A. M. (2019). Gas velocity structure of the Orion A integral-shaped filament. , 489(4):4771–4782.

Green, S., Montgomery, J. A., J., and Thaddeus, P. (1974). Tentative Identification of U93.174 as the Molecular Ion $N_2H\hat{\{}+\}$. , 193:L89.

Hacar, A., Clark, S. E., Heitsch, F., Kainulainen, J., Panopoulou, G. V., Seifried, D., and Smith, R. (2023). Initial Conditions for Star Formation: a Physical Description of the Filamentary ISM. In Inutsuka, S., Aikawa, Y., Muto, T., Tomida, K., and Tamura, M., editors, *Protostars and Planets VII*, volume 534 of *Astronomical Society of the Pacific Conference Series*, page 153.

Hacar, A. and Tafalla, M. (2011). Dense core formation by fragmentation of velocity-coherent filaments in L1517. , 533:A34.

Hacar, A., Tafalla, M., Forbrich, J., Alves, J., Meingast, S., Grossschedl, J., and Teixeira, P. S. (2018). An ALMA study of the Orion Integral Filament. I. Evidence for narrow fibers in a massive cloud. , 610:A77.

Haworth, T. J., Shima, K., Tasker, E. J., Fukui, Y., Torii, K., Dale, J. E., Takahira, K., and Habe, A. (2015). Isolating signatures of major cloud-cloud collisions - II. The lifetimes of broad bridge features. , 454(2):1634–1643.

Henshaw, J. D., Caselli, P., Fontani, F., Jiménez-Serra, I., and Tan, J. C. (2014). The dynamical properties of dense filaments in the infrared dark cloud G035.39-00.33. , 440(3):2860–2881.

Issac, N., Tej, A., Liu, T., and Wu, Y. (2020). G133.50+9.01: a likely cloud-cloud collision complex triggering the formation of filaments, cores, and a stellar cluster. , 499(3):3620–3629.

Jørgensen, J. K., Schöier, F. L., and van Dishoeck, E. F. (2004). Molecular inventories and chemical evolution of low-mass protostellar envelopes. , 416:603–622.

Kim, S., Lee, C. W., Tafalla, M., Gophinathan, M., Caselli, P., Myers, P. C., Chung, E. J., and Li, S. (2022a). The Role of Filamentary Structures in the Formation of Two Dense Cores, L1544 and L694-2. , 940(2):112.

Kim, S., Lee, C. W., Tafalla, M., Gophinathan, M., Caselli, P., Myers, P. C., Chung, E. J., and Li, S. (2022b). The Role of Filamentary Structures in the Formation of Two Dense Cores, L1544 and L694-2. , 940(2):112.

Klaassen, P. D., Johnston, K. G., Leurini, S., and Zapata, L. A. (2015). The SiO outflow from IRAS 17233-3606 at high resolution. , 575:A54.

Kong, S., Whitworth, D. J., Smith, R. J., and Hamden, E. T. (2022). Filament formation via collision-induced magnetic reconnection - formation of a star cluster. , 517(4):4679–4695.

Lada, C. J. and Lada, E. A. (2003). Embedded Clusters in Molecular Clouds. , 41:57–115.

Lee, Y.-N. and Hennebelle, P. (2016). Formation of a protocluster: A virialized structure from gravoturbulent collapse. I. Simulation of cluster formation in a collapsing molecular cloud. , 591:A30.

Leurini, S., Codella, C., Gusdorf, A., Zapata, L., Gómez-Ruiz, A., Testi, L., and Pillai, T. (2013). Evidence of a SiO collimated outflow from a massive YSO in IRAS 17233-3606. , 554:A35.

Leurini, S., Codella, C., Zapata, L., Beltrán, M. T., Schilke, P., and Cesaroni, R. (2011a). On the kinematics of massive star forming regions: the case of IRAS 17233-3606. , 530:A12.

Leurini, S., Gusdorf, A., Wyrowski, F., Codella, C., Csengeri, T., van der Tak, F., Beuther, H., Flower, D. R., Comito, C., and Schilke, P. (2014). Water emission from the high-mass star-forming region IRAS 17233-3606. , 564:L11.

Leurini, S., Hieret, C., Thorwirth, S., Wyrowski, F., Schilke, P., Menten, K. M., Güsten, R., and Zapata, L. (2008a). High-mass star formation in the IRAS 17233-3606 region: a new nearby and bright hot core in the southern sky. , 485(1):167–175.

Leurini, S., Hieret, C., Thorwirth, S., Wyrowski, F., Schilke, P., Menten, K. M., Güsten, R., and Zapata, L. (2008b). High-mass star formation in the IRAS 17233-3606 region: a new nearby and bright hot core in the southern sky. , 485(1):167–175.

Leurini, S., Pillai, T., Stanke, T., Wyrowski, F., Testi, L., Schuller, F., Menten, K. M., and Thorwirth, S. (2011b). The molecular distribution of the IRDC G351.77-0.51. , 533:A85.

Leurini, S., Schisano, E., Pillai, T., Giannetti, A., Urquhart, J., Csengeri, T., Casu, S., Cunningham, M., Elia, D., Jones, P. A., König, C., Molinari, S., Stanke, T., Testi, L., Wyrowski, F., and Menten, K. M. (2019). Characterising the high-mass star forming filament G351.776-0.527 with Herschel and APEX dust continuum and gas observations. , 621:A130.

Liu, H.-L., Sanhueza, P., Liu, T., Zavagno, A., Tang, X.-D., Wu, Y., and Zhang, S. (2020). Chemistry of Protostellar Clumps in the High-mass, Star-forming Filamentary Infrared Dark Cloud G034.43+00.24. , 901(1):31.

Liu, H.-L., Stutz, A., and Yuan, J.-H. (2019). Large-scale periodic velocity oscillation in the filamentary cloud G350.54+0.69. , 487(1):1259–1268.

Lu, X., Zhang, Q., Liu, H. B., Sanhueza, P., Tatematsu, K., Feng, S., Smith, H. A., Myers, P. C., Sridharan, T. K., and Gu, Q. (2018). Filamentary fragmentation and accretion in high-mass star-forming molecular clouds. *The Astrophysical Journal*, 855(1):9.

Mangum, J. G. and Shirley, Y. L. (2017). Corrigendum: How to Calculate Molecular Column Density. Publications of the Astronomical Society of the Pacific, Volume 129, Issue 976, pp. 069201 (2017).

Montillaud, J., Juvela, M., Vastel, C., He, J., Liu, T., Ristorcelli, I., Eden, D. J., Kang, S.-j., Kim, K.-T., Koch, P. M., Lee, C. W., Rawlings, M. G., Saajasto, M., Sanhueza, P., Soam, A., Zahorecz, S., Alina, D., Bögner, R., Cornu, D., Doi, Y., Malinen, J., Marshall, D. J., Micelotta, E. R., Pelkonen, V.-M., Viktor Tóth, L., Traficante, A., and Wang, K. (2019). Multi-scale analysis of the Monoceros OB 1 star-forming region. II. Colliding filaments in the Monoceros OB1 molecular cloud. , 631:A3.

Mori, S., Aikawa, Y., Oya, Y., Yamamoto, S., and Sakai, N. (2024). Synthetic Observations of the Infalling Rotating Envelope: Links between the Physical Structure and Observational Features. , 961(1):31.

Motte, F., Bontemps, S., Csengeri, T., Pouteau, Y., Louvet, F., Stutz, A. M., Cunningham, N., López-Sepulcre, A., Brouillet, N., Galván-Madrid, R., Ginsburg, A., Maud, L., Men'shchikov, A., Nakamura, F., Nony, T., Sanhueza, P., Álvarez-Gutiérrez, R. H., Armante, M., Baug, T., Bonfand, M., Busquet, G., Chapillon, E., Díaz-González, D., Fernández-López, M., Guzmán, A. E., Herpin, F., Liu, H. L., Olguin, F., Towner, A. P. M., Bally, J., Battersby, C., Braine, J., Bronfman, L., Chen, H. R. V., Dell'Ova, P., Di Francesco, J., González, M., Gusdorf, A., Hennebelle, P., Izumi, N., Joncour, I., Lee, Y. N., Lefloch, B., Lesaffre, P., Lu, X., Menten, K. M., Mignon-Risse, R., Molet, J., Moraux, E., Mundy, L., Nguyen Luong, Q., Reyes, N., Reyes Reyes, S. D., Robitaille, J. F., Rosolowsky, E., Sandoval-Garrido, N. A., Schuller, F., Svoboda, B., Tatematsu, K., Thomasson, B., Walker, D., Wu, B., Whitworth, A. P., and Wyrowski, F. (2022). ALMA-IMF. I. Investigating the origin of stellar masses: Introduction to the Large Program and first results. , 662:A8.

Motte, F., Bontemps, S., and Louvet, F. (2018). High-Mass Star and Massive Cluster Formation in the Milky Way. , 56:41–82.

Nony, T., Galván-Madrid, R., Motte, F., Pouteau, Y., Cunningham, N., Louvet, F., Stutz, A. M., Lefloch, B., Bontemps, S., Brouillet, N., Ginsburg, A., Joncour, I., Herpin, F., Sanhueza, P., Csengeri, T., Towner, A. P. M., Bonfand, M., Fernández-López, M., Baug, T., Bronfman, L., Busquet, G., Di Francesco, J., Gusdorf, A., Lu, X., Olguin, F., Valeille-Manet, M., and Whitworth, A. P. (2023). ALMA-IMF. V. Prestellar and protostellar core populations in the W43 cloud complex. , 674:A75.

Pagani, L., Daniel, F., and Dubernet, M.-L. (2008). On the frequency of N2H+ and N2D+. working paper or preprint.

Peretto, N. and Fuller, G. A. (2009). The initial conditions of stellar protocluster formation. I. A catalogue of Spitzer dark clouds. , 505(1):405–415.

Pouteau, Y., Motte, F., Nony, T., Galván-Madrid, R., Men'shchikov, A., Bontemps, S., Robitaille, J. F., Louvet, F., Ginsburg, A., Herpin, F., López-Sepulcre, A., Dell'Ova, P., Gusdorf, A., Sanhueza, P., Stutz, A. M., Brouillet, N., Thomasson, B., Armante, M., Baug, T., Bonfand, M., Busquet, G., Csengeri, T., Cunningham, N., Fernández-López, M., Liu, H. L., Olguin, F., Towner, A. P. M., Bally, J., Braine, J., Bronfman, L., Joncour, I., González, M., Hennebelle, P., Lu, X., Menten, K. M., Moraux, E., Tatematsu, K., Walker, D., and Whitworth, A. P. (2022). ALMA-IMF. III. Investigating the origin of stellar masses: top-heavy core mass function in the W43-MM2&MM3 mini-starburst. , 664:A26.

Pouteau, Y., Motte, F., Nony, T., González, M., Joncour, I., Robitaille, J. F., Busquet, G., Galván-Madrid, R., Gusdorf, A., Hennebelle, P., Ginsburg, A., Csengeri, T., Sanhueza, P., Dell'Ova, P., Stutz, A. M., Towner, A. P. M., Cunningham, N., Louvet, F., Men'shchikov, A., Fernández-López, M., Schneider, N., Armante, M., Bally, J., Baug, T., Bonfand, M., Bontemps, S., Bronfman, L., Brouillet, N., Díaz-González, D., Herpin, F., Lefloch, B., Liu, H. L., Lu, X., Nakamura, F., Nguyen-Luong, Q., Olguin, F., Tatematsu, K., and Valeille-Manet, M. (2023). ALMA-IMF. VI. Investigating the origin of stellar masses: Core mass function evolution in the W43-MM2&MM3 mini-starburst. , 674:A76.

Redaelli, E., Bizzocchi, L., Caselli, P., Sipilä, O., Lattanzi, V., Giuliano, B. M., and Spezzano, S. (2019). High-sensitivity maps of molecular ions in L1544. I. Deuteration of N_2H^+ and HCO^+ and primary evidence of N_2D^+ depletion. , 629:A15.

Reyes-Reyes, S. D., Stutz, A. M., Megeath, S. T., Xu, F., Álvarez-Gutiérrez, R. H., Sandoval-Garrido, N., and Liu, H. L. (2024). Benchmarking the IRDC G351.77-0.53: Gaia DR3 distance, mass distribution, and star formation content. .

Sabatini, G., Giannetti, A., Bovino, S., Brand, J., Leurini, S., Schisano, E., Pillai, T., and Menten, K. M. (2019). On the size of the CO-depletion radius in the IRDC G351.77-0.51. , 490(4):4489–4501.

Schwarz, K. R., Teague, R., and Bergin, E. A. (2019). Line Ratios Reveal N_2H^+ Emission Originates above the Midplane in TW Hydrae. , 876(1):L13.

Shirley, Y. L. (2015). The Critical Density and the Effective Excitation Density of Commonly Observed Molecular Dense Gas Tracers. , 127(949):299.

Stutz, A. M., Gonzalez-Lobos, V. I., and Gould, A. (2018). Gaia: Orion's integral shaped filament is a standing wave.

Stutz, A. M. and Gould, A. (2016). Slingshot mechanism in Orion: Kinematic evidence for ejection of protostars by filaments. , 590:A2.

Tafalla, M. and Hacar, A. (2014). Chains of Dense Cores in the Taurus L1495/B213 Complex. In *Dense Cores: Origin, Evolution, and Collapse*, volume 4, page 103.01.

Thaddeus, P. and Turner, B. E. (1975). Confirmation of interstellar N_2H^+. , 201:L25–L26.

Tobin, J. J., Bergin, E. A., Hartmann, L., Lee, J.-E., Maret, S., Myers, P. C., Looney, L. W., Chiang, H.-F., and Friesen, R. (2013). Resolved Depletion Zones and Spatial Differentiation of N_2H^+ and N_2D^+. , 765(1):18.

Tobin, J. J., Hartmann, L., Bergin, E., Chiang, H.-F., Looney, L. W., Chandler, C. J., Maret, S., and Heitsch, F. (2012). Complex structure in class 0 protostellar envelopes. iii. velocity gradients in non-axisymmetric envelopes, infall, or rotation?*. *The Astrophysical Journal*, 748(1):16.

Towner, A. P. M., Ginsburg, A., Dell'Ova, P., Gusdorf, A., Bontemps, S., Csengeri, T., Galván-Madrid, R., Louvet, F. K., Motte, F., Sanhueza, P., Stutz, A. M., Bally, J., Baug, T., Chen, H. R. V., Cunningham, N., Fernández-López, M., Liu, H. L., Lu, X., Nony, T., Valeille-Manet, M., Wu, B., Álvarez-Gutiérrez, R. H., Bonfand, M., Di Francesco, J., Nguyen-Luong, Q., Olguin, F., and Whitworth, A. P. (2023). ALMA-IMF IX: Catalog and Physical Properties of 315 SiO Outflow Candidates in 15 Massive Protoclusters. *arXiv e-prints*, page arXiv:2310.13125.

Turner, B. E. (1974). U93.174: a New Interstellar Line with Quadrupole Hyperfine Splitting. , 193:L83.

van 't Hoff, M. L. R., Walsh, C., Kama, M., Facchini, S., and van Dishoeck, E. F. (2017). Robustness of N_2H^+ as tracer of the CO snowline. , 599:A101.

Yu, N.-P., Xu, J.-L., Wang, J.-J., and Liu, X.-L. (2018). Chemical evolution of n2h+ in six massive star-forming regions. *The Astrophysical Journal*, 865(2):135.

Zapata, L. A., Leurini, S., Menten, K. M., Schilke, P., Rolffs, R., and Hieret, C. (2008). Unveiling a Compact Cluster of Massive and Young Stars in IRAS 17233-3606. , 136(4):1455–1462.

Zhou, J.-W., Liu, T., Evans, N. J., Garay, G., Goldsmith, P. F., Gómez, G. C., Vázquez-Semadeni, E., Liu, H.-L., Stutz, A. M., Wang, K., Juvela, M., He, J., Li, D., Bronfman, L., Liu, X., Xu, F.-W., Tej, A., Dewangan, L. K., Li, S., Zhang, S., Zhang, C., Ren, Z., Tatematsu, K., Shing Li, P., Won Lee, C., Baug, T., Qin, S.-L., Wu, Y., Peng, Y., Zhang, Y., Liu, R., Luo, Q.-Y., Ge, J., Saha, A., Chakali, E., Zhang, Q., Kim, K.-T., Ristorcelli, I., Shen, Z.-Q., and Li, J.-Z. (2022). ATOMS: ALMA Three-millimeter Observations of Massive Star-forming regions - XI. From inflow to infall in hub-filament systems. , 514(4):6038–6052.

Appendix A

PySpecKit experiment

To know the performance of PySpecKit and the SNR threshold at which it provides good results, we applied the following test: It consists in selecting a single spectra from the original data to fit it employing PySpecKit (with guesses and limits defined), obtaining a model and their respective parameters (input model). Then, we have created a grid with this model assigning a different SNR for each spectra. This grid is fitted by PySpecKit (with the same guesses and limits as before) obtaining a new model for each spectra (output models). This way, we can compare the first parameters returned from the single spectra versus the parameters returned from the grid. We have applied this on different spectra from the original data and fitting one and two velocity components. The result of this experiment are consistent whether it's fitting one velocity component or fitting two velocity component, which show that at SNR > 9 PySpecKit returns reliable values.

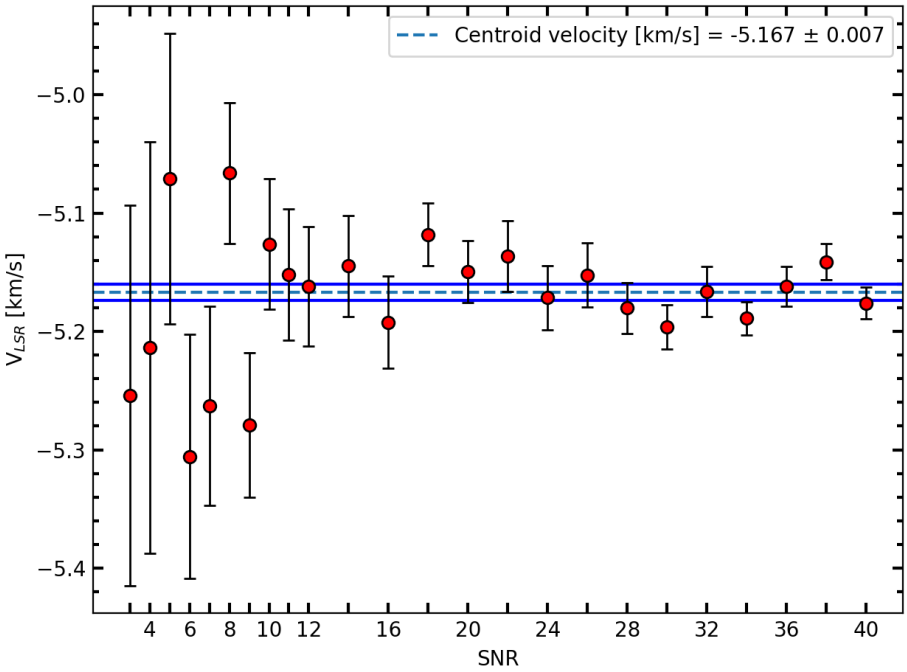

Figure A.0.1: The red points represent the centroid velocity value of the output models. The blue dashed line shows the centroid velocity of the input model and the blue solid line represent the associated errors. The error values increase while lower is the SNR value and the centroid velocity value of the output models are moving away from the input model as we expected.

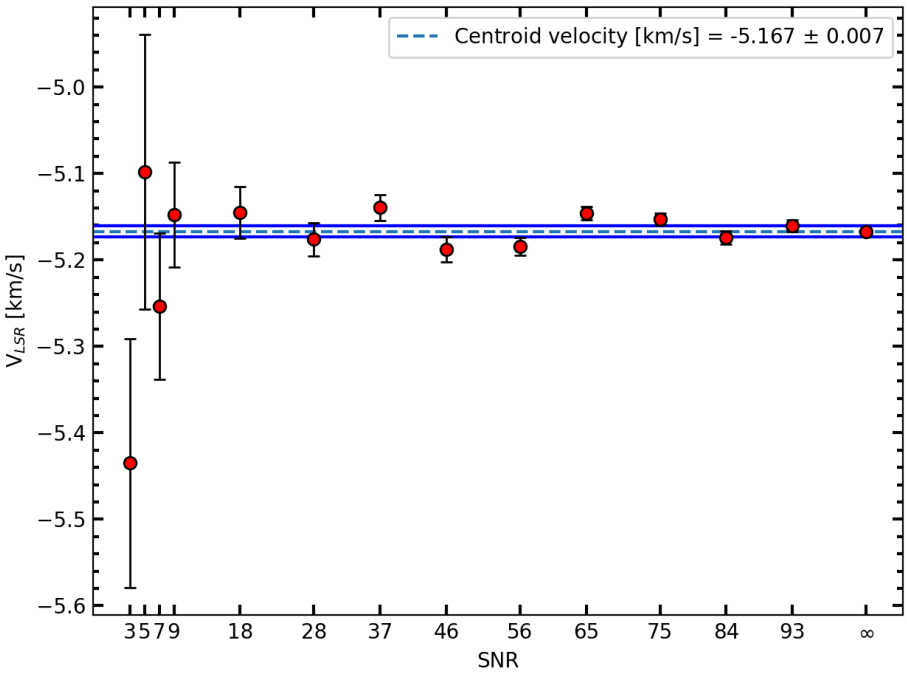

Figure A.0.2: Same caption as Fig. A.0.1.

Appendix B

Good and bad fitting examples

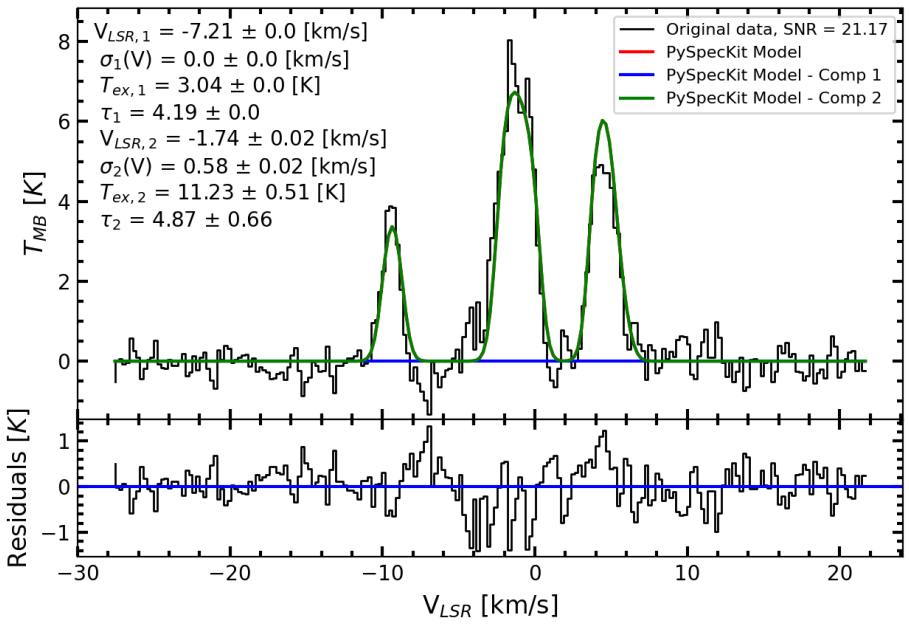

Figure B.0.1: The green line represent the spectra of the second-velocity-component fitted by PySpecKit, which is overlapping the red line. The blue line represent the spectra of the first-velocity-component fitted by PySpecKit. The first modeled component present a $\sigma_1(V) = 0$ km/s, without uncertainties in its parameters.

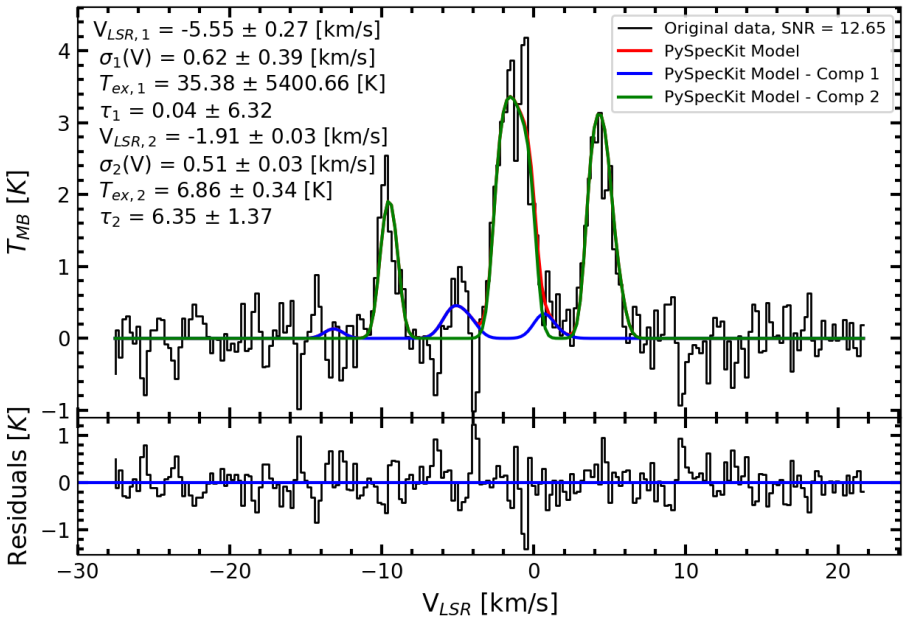

Figure B.0.2: The green line represent the spectra of the second-velocity-component fitted by PySpecKit. The blue line represent the spectra of the first-velocity-component fitted by PySpecKit, whose intensity is similar as what we measure for noise. This produce bad estimation values and considerable uncertainties.

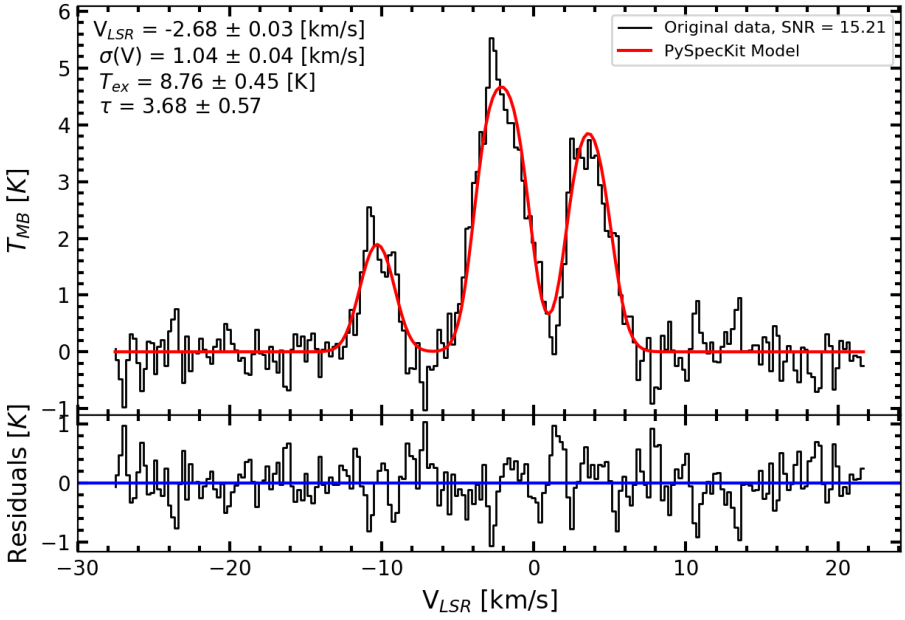

Figure B.0.3: The red line represents the model spectra fitted by PySpecKit.

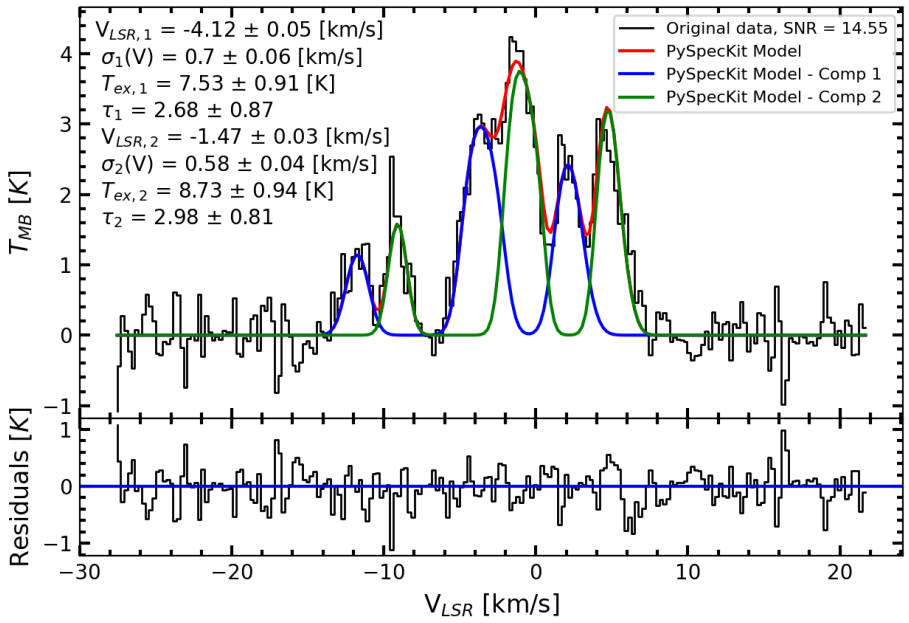

Figure B.0.4: The blue and green lines represent the first- and the second-velocity-component fitted by PySpecKit. The red line represents the model adding both velocity components.

Appendix C

Infalling and rotating sphere model

The sphere is under gravitational infall and keplerian rotation, its respective velocities are described by equation (1) and (2). It has a density profile that follows a power law described in equation (3)

$$V_{\rm in} = \sqrt{\frac{2GM}{r}} \tag{C.0.1}$$

$$V_{\rm rot} = \sqrt{\frac{GM}{r}} \tag{C.0.2}$$

$$\rho(r) = \rho_0 \left(\frac{r}{\rm pc}\right)^{-\gamma} \tag{C.0.3}$$

where r is the radius of the sphere, G is the gravitational constant, M is the enclosed mass, and ρ_0 is a known density. To generate a infalling and rotating sphere model, we utilize $r = 0.8$ pc, and $\gamma = 3.1$. The total mass utilized is 270 $M_\odot$ and 2700 $M_\odot$, deriving $\rho_0 = 3.466$ $M_\odot/pc^3$ and $\rho_0 = 34.66$ $M_\odot/pc^3$, respectively. Although the features observed in the PV-diagram are not affected by the mass, the velocities present differences.

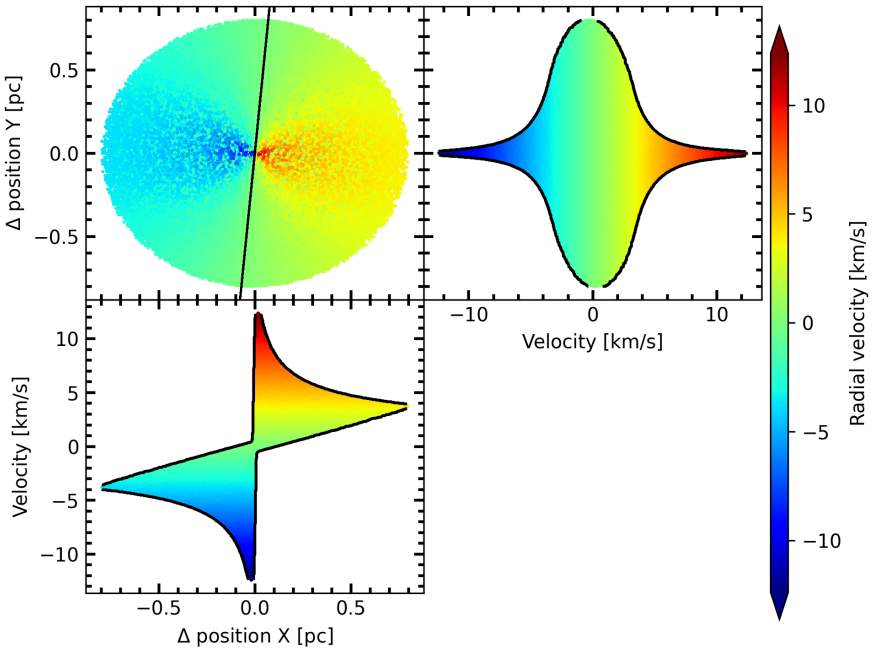

Figure C.0.1: PV-diagram of a rotating sphere model. The velocities represent the radial velocities derived from the Eq. C.0.2. The black solid line represent the rotating axis, which is inclined 85° respect to the x axis.

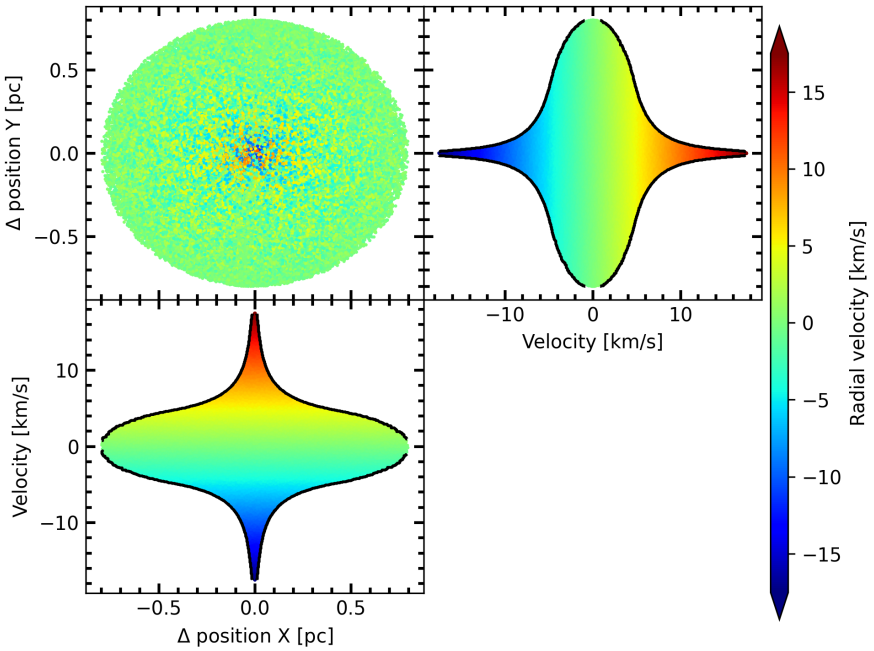

Figure C.0.2: PV-diagram of an infalling sphere model. The velocities represent the radial velocities derived from the Eq. C.0.1.

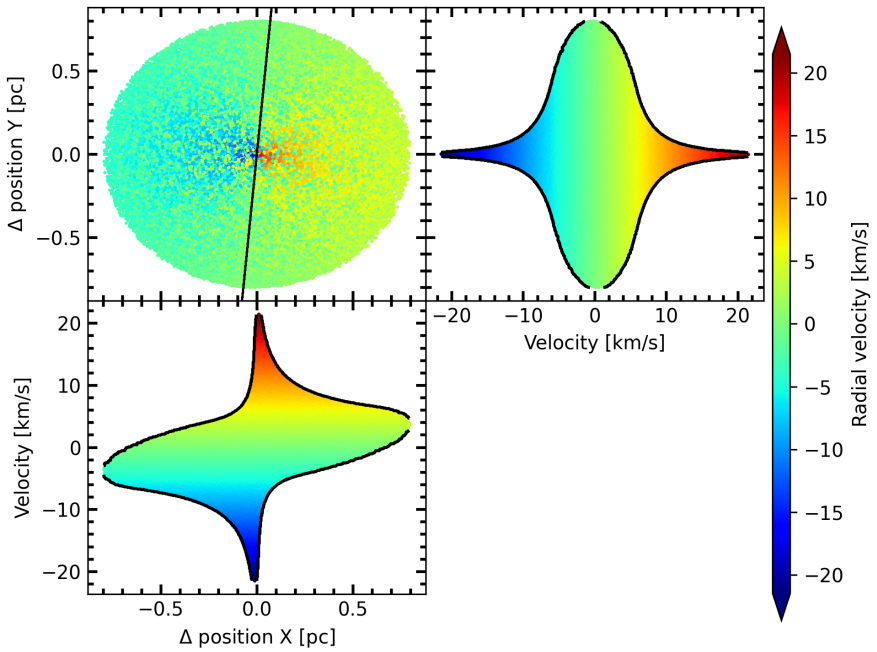

Figure C.0.3: PV-diagram of an infalling and rotating sphere model. The velocities represent the radial velocities derived from the Eq. C.0.1 plus the Eq. C.0.2. The black solid line represent the rotating axis, which is inclined 85° respect to the x axis.

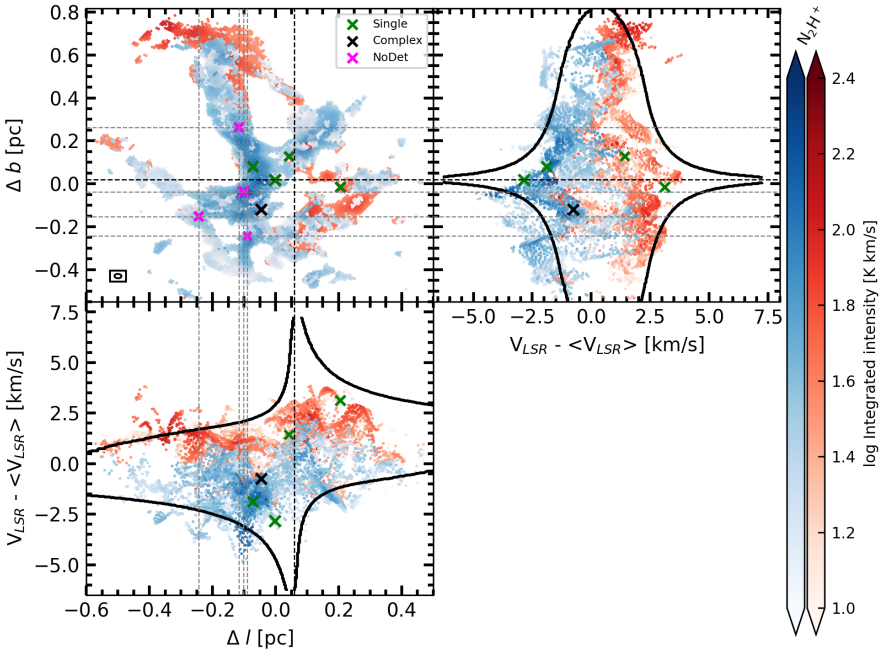

Figure C.0.4: PV-diagram of N_2H^+ emission in G351.77 protocluster. The black contour represents the features for an infalling and rotating sphere model, whose mass is 270 $M_\odot$.

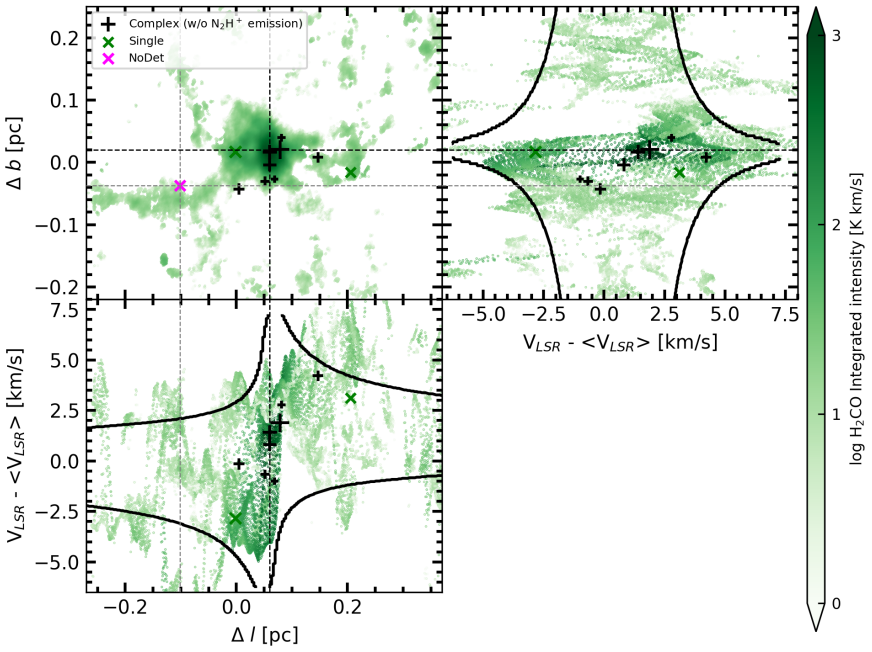

Figure C.0.5: PV-diagram of H_2CO emission in G351.77 protocluster. The black contour represents the features for an infalling and rotating sphere model, whose mass is 270 $M_\odot$.

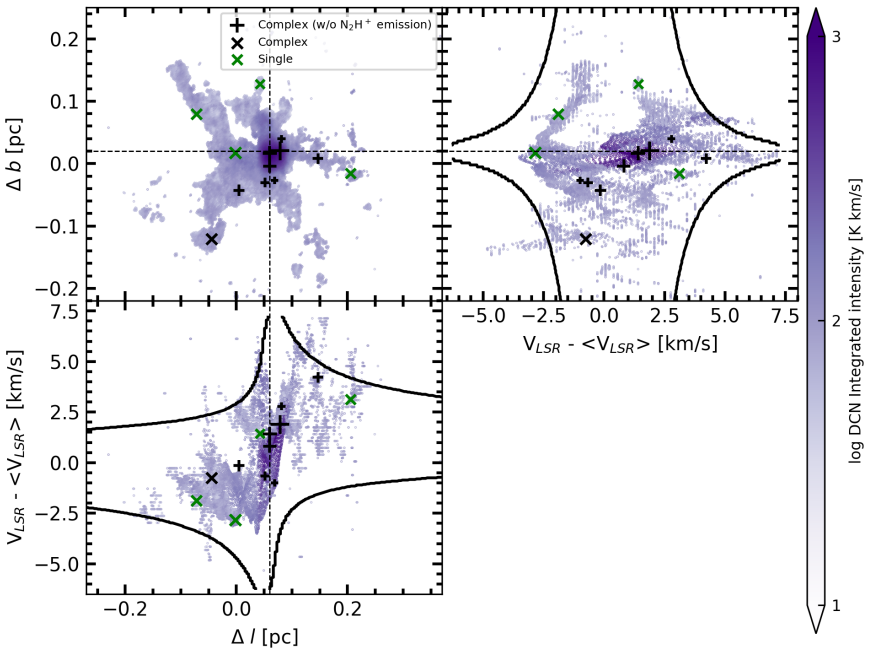

Figure C.0.6: PV-diagram of DCN emission in G351.77 protocluster. The black contour represents the features for an infalling and rotating sphere model, whose mass is 270 $M_\odot$.

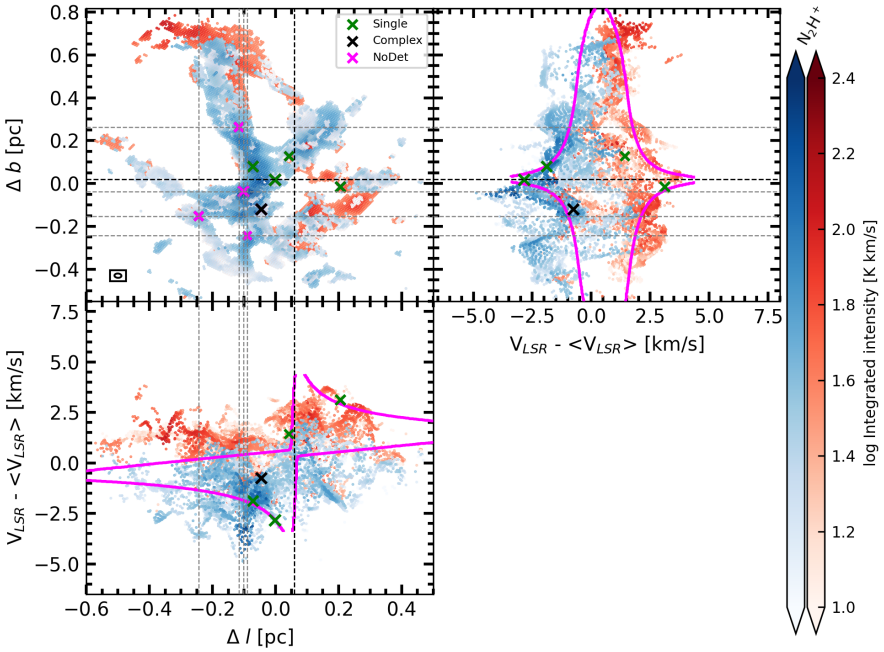

Figure C.0.7: PV-diagram of N_2H^+ emission in G351.77 protocluster. The magenta contour represents the features for a rotating sphere model, whose mass is 270 $M_\odot$.

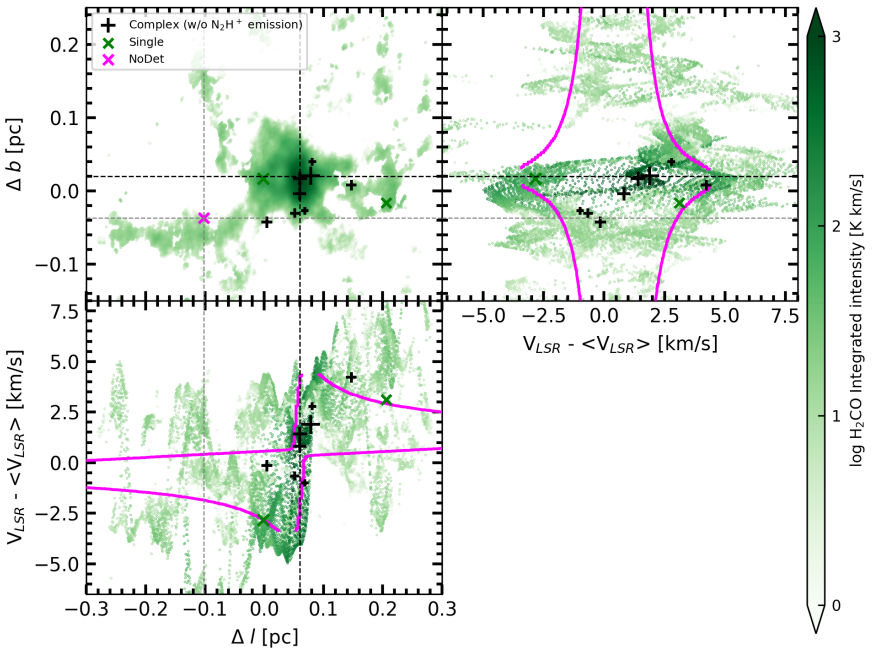

Figure C.0.8: PV-diagram of H_2CO emission in G351.77 protocluster. The magenta contour represents the features for a rotating sphere model, whose mass is 270 $M_\odot$.

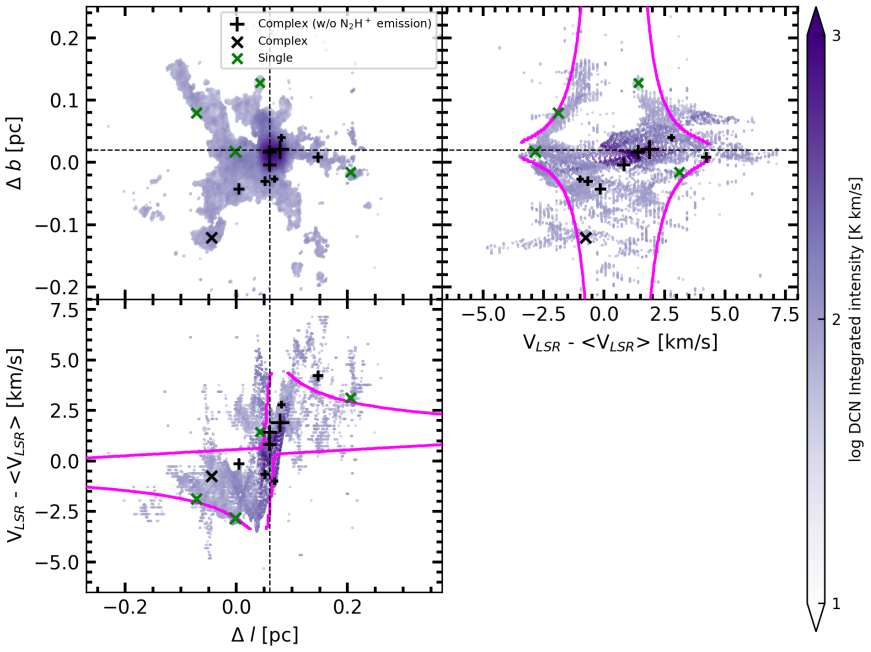

Figure C.0.9: PV-diagram of DCN emission in G351.77 protocluster. The magenta contour represents the features for a rotating sphere model, whose mass is 270 $M_{\odot}$.

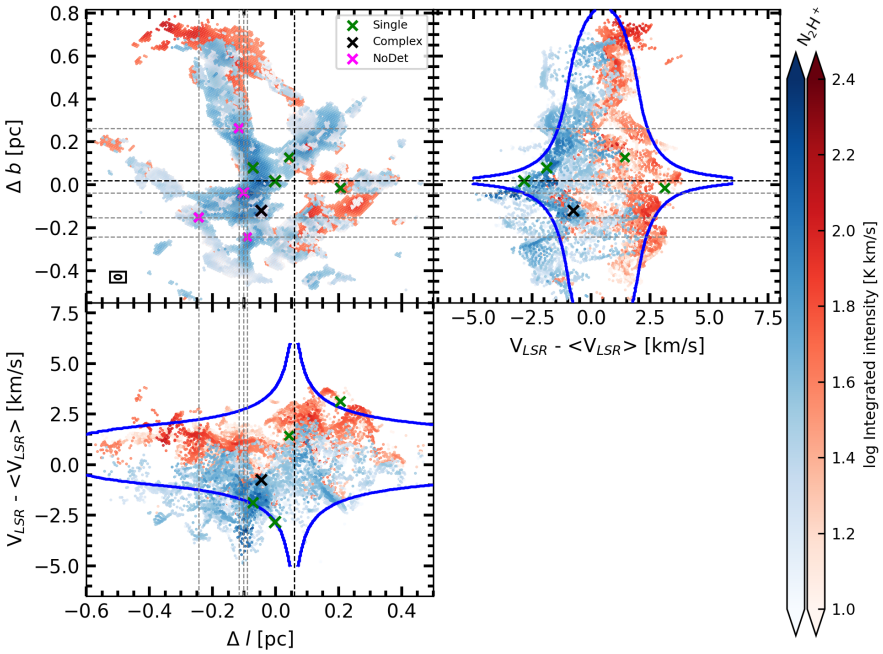

Figure C.0.10: PV-diagram of N_2H^+ emission in G351.77 protocluster. The blue contour represents the features for an infalling sphere model, whose mass is 270 $M_{\odot}$.

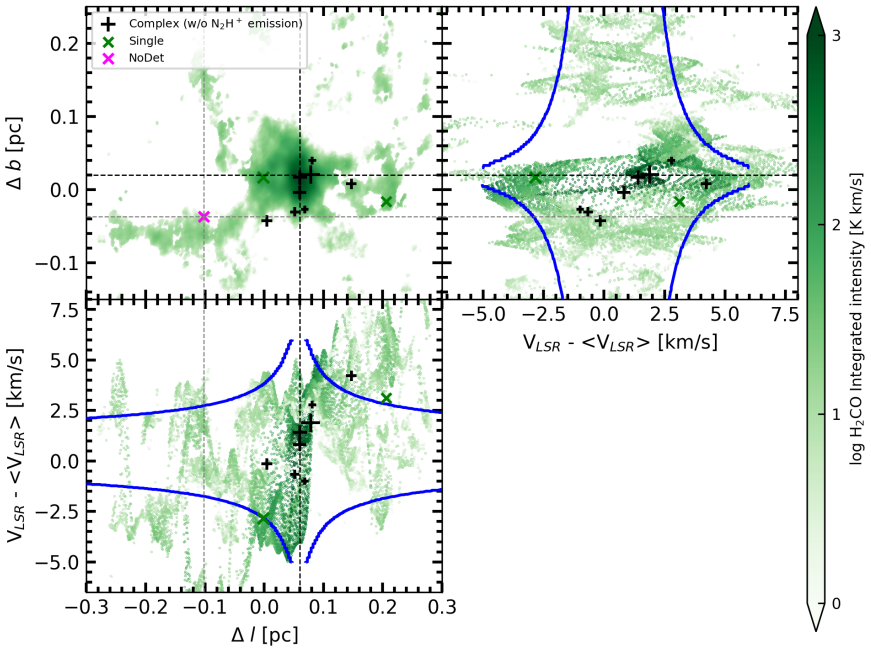

Figure C.0.11: PV-diagram of H_2CO emission in G351.77 protocluster. The blue contour represents the features for an infalling sphere model, whose mass in 270 $M_\odot$.

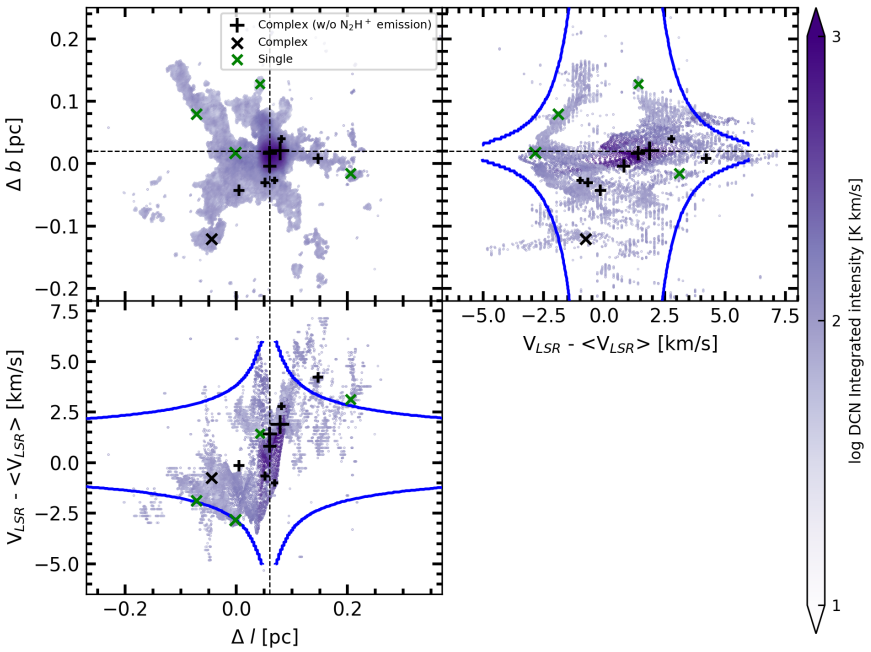

Figure C.0.12: PV-diagram of DCN emission in G351.77 protocluster. The blue contour represents the features for an infalling sphere model, whose mass is 270 $M_\odot$.